antioxidants

MDPI

Article

FNB Modulates Oxidative Stress Induced by PRV Infection in RAW 264.7 Cells Through the Mir22hg/miR-365-2-5p/iNOS ceRNA Regulatory Axis

Yuheng Wei †, Wen Zhao †, Haifeng Yuan, Qi Chen, Xiaoli Yu, Qiuhua Wang, Meiling Yu * and Tingjun Hu *

College of Animal Science and Technology, Guangxi University, Nanning 530004, China
* Correspondence: yumeiling@gxu.edu.cn (M.Y.); tingjunhu@gxu.edu.cn (T.H.); Tel.: +86-771-3235635 (T.H.); Fax: +86-771-3270149 (T.H.)
† These authors contributed equally to this work.

Abstract

Infection with pseudorabies virus (PRV) can induce intense oxidative stress. The normal butanol fraction of flavonoids extracted from *Polygonum hydropiper* L. (FNB) shows substantial antioxidant activity. However, the molecular mechanisms through which FNB affects oxidative stress caused by PRV infection remain unclear; moreover, how noncoding RNAs influence this process is unknown. Therefore, based on whole-transcriptome sequencing, we propose the following hypothesis: FNB regulates oxidative stress generated in PRV-infected RAW 264.7 cells through the ceRNA regulatory axis. The results showed that 3549 mRNAs, 62 miRNAs, and 1263 lncRNAs exhibited differential expression in PRV-infected RAW 264.7 cells; in contrast, 1427 mRNAs, 11 miRNAs, and 460 lncRNAs displayed differential expression in FNB-treated PRV-infected RAW 264.7 cells. According to Gene Ontology and Kyoto Encyclopedia of Genes and Genomes analyses, the differentially expressed genes (DEGs) exhibited remarkable enrichment in signaling pathways such as TNF, NF-κB, IL-17, and Toll-like receptors. Based on the DEGs in these pathways, a Mir22hg/miR-365-2-5p/iNOS ceRNA regulatory axis was constructed. The lncRNA Mir22hg is localized in the cytoplasm. Interference or overexpression of Mir22hg can significantly regulate oxidative stress induced by PRV infection by controlling Nrf2/HO-1 signaling pathway activation. Specifically, Mir22hg overexpression markedly upregulated the levels of iNOS, ROS, and NO and remarkably downregulated HO-1, Nrf2, and NQO1 mRNA and protein expression levels; however, Mir22hg interference yielded opposite results. Rescue experiments further indicated that simultaneous miR-365-2-5p interference or overexpression could reverse the effects of Mir22hg interference or overexpression, thereby regulating ROS and NO levels and Nrf2/HO-1 signaling pathway activation. Finally, we identified all flavonoid monomers in FNB by using Flavonoid-Targeted Metabolomics technology, providing a new perspective for utilizing plant flavonoids to prevent PRV infection.

Keywords: n-butanol fraction of flavonoids from *Polygonum hydropiper* L.; oxidative stress; pseudorabies virus; ceRNA

Check for updates

Academic Editor: Janusz M. Gebicki

Received: 10 October 2026
Revised: 3 November 2026
Accepted: 5 November 2026
Published: 8 November 2026

Copyright: © 2026 by the authors. Licensee MDPI, Basel, Switzerland. This article is an open access article distributed under the terms and conditions of the Creative Commons Attribution (CC BY) license.

1. Introduction

Pseudorabies virus (PRV), or *Suid alphaherpesvirus* 1, an etiological agent of Aujeszky's disease, belongs to the subfamily Alphaherpesvirinae. It has a wide host range, with pigs as its only natural host [1]. Following PRV infection, sows exhibit reproductive failure, fattening pigs show dyspnea and growth retardation, and newborn piglets develop fatal

encephalitis [1]. Other susceptible animals, such as mice, rats, cats, and dogs, usually die following infection [2]. In the porcine kidney cell line (PK-15), PRV infection markedly increases reactive oxygen species (ROS) levels, induces severe oxidative stress, triggers mitophagy, reduces mitochondrial abundance in a time- and dose-dependent manner, suppresses interferon response, and enhances the replication of the virus [3]. PRV infection remains a major concern for the global swine industry. China, the largest producer and consumer of pork globally, has experienced two major PRV epidemics: the first was triggered by classical PRV strains, and the second occurred due to PRV variant strains in 2011 [4]. Previous studies have reported that PRV variant strains show higher virulence in pigs compared to classical PRV strains. Although Bartha-K61, the traditional vaccine strain, may induce total protection against classical PRV strains, it does not offer sufficient protection against variant strains [5]. In 2019, the first PRV strain (hSD-1/2019) in humans was obtained from a patient's cerebrospinal fluid [6]. Because of the increasing worldwide prevalence of PRV infection in pigs, this "new fatal zoonotic disease" requires greater focus.

Polygonum hydropiper L. flavonoids are natural bioactive components extracted from the plant *P. hydropiper* L. (Polygonaceae), and they exhibit substantial antibacterial, insecticidal, antiviral, and antioxidant activities [7]. According to previous studies, the normal butanol fraction of flavonoids from *P. hydropiper* L. (FNB) can reduce excessive ROS production, enhance superoxide dismutase and catalase activities, and upregulate *HO-1* and *Nrf2* mRNA and HO-1 and Nrf2 protein expression, thereby counteracting oxidative stress due to viral infection in RAW 264.7 cells [8]. By conducting high-performance liquid chromatography (HPLC), Tao et al. [9] found that FNB contains quercitrin, quercetin, and rutin and thus shows stronger antioxidant effects compared to vitamin C. However, all flavonoid components in FNB have not yet been fully elucidated since no flavonoid database has been established.

MicroRNA (miRNA), a type of noncoding RNA, is typically approximately 22 nucleotides in length. It can bind to target mRNA, thereby inhibiting gene translation or promoting mRNA degradation [10]. Long noncoding RNA (lncRNA) regulates target mRNA transcription by binding competitively to downstream miRNA response elements, a mechanism known as competitive endogenous RNA (ceRNA) [11]. Generally, in this mechanism, lncRNA expression levels are consistent with those of target mRNA, whereas miRNA expression levels are opposite to those of lncRNA and target mRNA. *LINC01002*, acting as a ceRNA, promotes inflammation and oxidative stress induced by COVID-19 by sponging *miR-4324* to regulate *FRMD8* [12]. Additionally, the flavonoid monomer quercetin can inhibit inflammation and oxidative stress induced by caerulein by targeting *MAP2K6* and lncRNA *NEAT1* to regulate *miR-216b* [13].

Oxidative stress develops following the disturbed homeostasis of overproduction of free radicals and weakened antioxidant defense, which disrupts redox signaling and control processes and induces molecular damage [14]. The reaction of nitric oxide (NO) with superoxide radicals can generate peroxynitrite ($ONOO^-$), a strong oxidant produced in activated macrophages. It not only causes severe oxidative stress but also damages biomolecules such as proteins and DNA [15]. The Nrf2/HO-1 antioxidant axis is a key pathway employed by cells to eliminate excessive ROS accumulation. Wei et al. [8,16] showed that FNB can downregulate the expression of *iNOS* mRNA and iNOS protein, upregulate *HO-1* and *Nrf2* mRNA and HO-1 and Nrf2 protein expression, and reduce ROS and NO overproduction, thereby modulating oxidative stress due to viral infection in RAW 264.7 cells. Despite this positive outcome, no study has clarified the molecular mechanisms through which FNB exerts its antioxidant effects. Therefore, based on our whole-transcriptome sequencing data, we proposed the following hypothesis: FNB influences oxidative stress triggered by PRV infection in RAW 264.7 cells through the ceRNA regulatory axis. The present study was

conducted to lay a foundation for using plant flavonoids in preventing and treating viral infections in animals.

2. Materials and Methods

2.1. Experimental Materials

Fetal bovine serum (FBS) was provided by VivaCell (Shanghai, China). Opti-MEM and DMEM were bought from Gibco (Shanghai, China). TRIzol reagent was obtained from Takara (Dalian, China), and 2× Universal SYBR Green qPCR Mix and SPARKscript II All-in-one RT SuperMix for qPCR were supplied by SparkJade (Jinan, China). Promega (Madison, WI, USA) provided the Dual-Luciferase Reporter Assay System. Lipofectamine 2000 was supplied by Thermo Fisher Scientific (Shanghai, China). Ultra-sensitive ECL Chemiluminescence Kit, primary antibodies (anti-iNOS rabbit pAb (1:1000 dilution; GB115703-100), anti-NRF2 rabbit pAb (1:1000 dilution; GB113808-100), anti-heme oxygenase 1 rabbit pAb (1:1000 dilution; GB115713-50), anti-NQO1 rabbit pAb (1:1000 dilution; GB11282-100), and recombinant anti-β-actin antibody (rabbit mAb) (1:3000 dilution; GB15003-100)), and secondary antibodies (HRP-tagged goat anti-rabbit IgG (H + L) (GB23303, 1:10,000 dilution)) were procured from Servicebio (Wuhan, China). Sangon Biotech (Shanghai, China) conducted DNA primer synthesis and sequencing.

We commissioned OBiO Technology (Shanghai) Corp., Ltd. (Shanghai, China) to synthesize the full-length gene sequence of mouse lncRNA *Mir22hg*. The plasmid vector used was the common eukaryotic fluorescent vector pcDNA3.1-CMV-MCS-hGHpolya-EF1a-EGFP. The synthesized plasmid was sequenced. Following validation that the plasmid contained the lncRNA *Mir22hg* gene sequence, the lncRNA *Mir22hg* plasmid and the empty pcDNA3.1 vector were separately extracted and purified. The resulting plasmids were designated oe-Mir22hg and oe-NC, respectively. The siRNA targeting lncRNA *Mir22hg* was also designed and synthesized by OBiO Technology (Shanghai) Corp., Ltd.

2.2. Cell Details and Virus

RAW 264.7 cells and Porcine Kidney-15 (PK-15) cells were provided by Procell Life Science & Technology Co., Ltd. (Wuhan, China), with original sources from the American Type Culture Collection (ATCC). The RRID for PK-15 cells is CVCL_2160, and the RRID for RAW264.7 cells is CVCL_0493.

The Department of Preventive Veterinary Medicine, College of Animal Science and Technology, Guangxi University, isolated and verified the PRV strain GXLB-2013. This strain was subsequently amplified in PK-15 cells and stored in an ultra-low-temperature freezer at −80 °C by the Basic Pharmacology Laboratory, College of Animal Science and Technology, Guangxi University. This strain had a TCID50 value of $10^{6.71}$/0.1 mL.

2.3. Flavonoid-Targeted Metabolomics

FNB was prepared by the Basic Pharmacology Laboratory. The total flavonoid content was estimated to be 55.3%. Using the targeted flavonoid metabolite detection library established by Sanshubio, metabolites in the samples were detected by ultra-HPLC-tandem electrostatic field orbital ion trap mass spectrometry (UHPLC-Q Exactive HFX, Thermo Fisher Scientific, Waltham, MA, USA). By constructing standard curves and comparing the retention times and molecular masses (mass error < 10 ppm) with 386 flavonoid monomer standards, the metabolites in FNB were qualitatively and quantitatively analyzed. Detailed experimental methods are provided in Supplementary Materials.

2.4. Sample Preparation for RNA Sequencing (RNA-Seq)

After seeding into 6-well plates, RAW264.7 cells were subjected to 24 h incubation at 37 °C in 5% CO_2. When the cell confluence reached approximately 80%, cells in the PRV group and PRV + FNB group were exposed to PRV (MOI = 1) at 37 °C for 2 h. Thereafter, the PRV + FNB group was treated with FNB at a concentration of 50 μg/mL for 12 h. Following supernatant removal and 3 rounds of washing with PBS, TRIzol reagent (1 mL) was added to each well for RNA extraction. RNA sample quality was examined before RNA-seq.

2.5. RNA-Seq

The experimental procedure for whole-transcriptome sequencing was as follows. The mirVana miRNA Isolation Kit (Ambion, Thermo Fisher Scientific, Austin, TX, USA) was utilized for extracting total RNA in accordance with the manufacturer's instructions. RNA integrity was confirmed with the Agilent 2100 Bioanalyzer (Agilent Technologies, Santa Clara, CA, USA). Only those samples with an RNA Integrity Number of ≥7 were retained for subsequent analyses. TruSeq Stranded Total RNA with Ribo-Zero Gold was employed for constructing libraries by following the recommended protocol. Sequencing of the libraries was conducted on the Illumina sequencing platform (HiSeq™ 2500), which generated 150 bp/125 bp paired-end reads. RNA library sequencing was performed on HiSeq™ 2500 by Shanghai OE Biotech Co., Ltd. (Shanghai, China). The RNA-seq raw data presented in this study have been deposited in the Genome Sequence Archive (GSA), National Genomics Data Center, China National Center for Bioinformation/Beijing Institute of Genomics, Chinese Academy of Sciences (Genomics, Proteomics & Bioinformatics 2025; Nucleic Acids Research 2025). The accession number is CRA044205, and the data are publicly available at https://ngdc.cncb.ac.cn/gsa accessed on 15 October 2026.

2.6. Construction of the ceRNA Regulatory Axis

To clarify the relationship between differentially expressed (DE) miRNAs, mRNAs, and lncRNAs in the Control, PRV, and PRV_FNB groups, we developed a ceRNA regulatory axis through Kyoto Encyclopedia of Genes and Genomes (KEGG) and Gene Ontology (GO) analyses. We exclusively examined DE mRNAs in the NF-κB signaling pathway and predicted the miRNAs targeting these mRNAs by using the miRanda database (https://tools4mirs.org/software/target_prediction/miranda/ accessed on 15 October 2026). The miRTarBase database (https://awi.cuhk.edu.cn/miRTarBase/ accessed on 15 October 2026) was also utilized for predicting DE lncRNAs that showed targeted binding to the candidate miRNAs and exhibited negatively correlated expression levels with them. Finally, Cytoscape software (version 3.10.5) (National Resource for Network Biology) was employed for visualizing the constructed ceRNA network.

2.7. RNA Fluorescence In Situ Hybridization (FISH)

RAW 264.7 cell-climbing slides were fixed with acetone for 5 min at −20 °C and subsequently washed three times with PBS (pH 7.4) (5 min/cycle) on a destaining shaker. Following the dropwise addition of pre-hybridization solution, the slides were maintained for 1 h at 40 °C. After the pre-hybridization solution was discarded, the hybridization solution supplemented with the lncRNA probe was added dropwise, followed by overnight hybridization in a constant-temperature incubator. After hybridization, the hybridization solution was washed off. The slides were then treated with 2× SSC (10 min, 40 °C); 1× SSC twice (5 min each, 40 °C); and 0.5× SSC (10 min, room temperature). Subsequently, under light-protected conditions, 1× DAPI staining solution was added dropwise to counterstain the nuclei, followed by incubation for 8 min in the dark. After rinsing, the slides were

sealed with dropwise addition of anti-fade mounting medium. Finally, slide observation and image acquisition were performed under a Nikon upright fluorescence microscope (CY3 red fluorescence: excitation and emission wavelengths: 535 and 590 nm, respectively, emitting red light).

2.8. Knockdown of lncRNA Mir22hg and miRNA miR-365-2-5p in RAW 264.7 Cells

RAW 264.7 cells were grown to achieve 80% confluence. After discarding the supernatant, the cells were washed three times with PBS. The culture medium was then replaced with OPTI-MEM. The experimental design included two optional grouping schemes: one scheme comprised 3 groups, namely Control, si-NC + PRV, and si-Mir22hg + PRV or Control, si-NC + PRV + FNB, and si-Mir22hg + PRV + FNB; the other scheme comprised 6 groups, namely Control, si-NC + PRV/PRV + FNB, si-Mir22hg + PRV/PRV + FNB, inhibitor-NC + PRV/PRV + FNB, inhibitor-miR362-2-5p + PRV/PRV + FNB, and si-Mir22hg + inhibitor-miR362-2-5p + PRV/PRV + FNB. Lipofectamine^{TM} 2000 was utilized for performing all transfections, and the cells were grown at 37 °C for further analyses. The siRNAs for *Mir22hg*, si-NC, *miR-365-2-5p* inhibitor, and inhibitor-NC were designed and synthesized by OBiO Technology (Shanghai) Corp., Ltd. The target sequence of *miR-365-2-5p* was 5′-AGGGACTTTCAGGGGCAGCTGTG-3′. The following siRNA sequences for *Mir22hg* were used: si-Mir22hg-1 (sense strand: GCUCCUCUGUCCACAGCAATT, antisense strand: UUGCUGUGGACAGAGGAGCTT), si-Mir22hg-2 (sense strand: GGUCAGAGAGGCACGUAGATT, antisense strand: UCUACGUGCCUCUCUGACCTT), si-Mir22hg-3 (sense strand: GGUUAGUAAUUCAAAGAAATT, antisense strand: UUUCUUUGAAUUACUAACCTT), and si-NC (sense strand: UUCUCCGAACGUGUCACGUTT, antisense strand: ACGUGACACGUUCGGAGAATT). si-Mir22hg-2 showed the best interference efficiency; therefore, in subsequent experiments, "si-Mir22hg" refers to transfection with si-Mir22hg-2.

2.9. Overexpression of lncRNA Mir22hg and miRNA miR-365-2-5p in RAW 264.7 Cells

The overexpression plasmid is described in Section 2.1. *miR-365-2-5p* mimics and mimics-NC were simultaneously designed and synthesized by OBiO Technology (Shanghai) Corp., Ltd. The experimental groupings and procedures are similar to or consistent with those described in Section 2.8.

2.10. Dual-Luciferase Reporter Assay

The binding sites between iNOS and miR-365-2-5p as well as between miR-365-2-5p and Mir22hg were predicted using miRanda. The experimental plasmids—pMIR-REPORT Luciferase-NOS2 3′UTR (MUT), pMIR-REPORT Luciferase-NOS2 3′UTR (WT), pMIR-REPORT Luciferase-Mir22hg (MUT), and pMIR-REPORT Luciferase-Mir22hg (WT)—were constructed by OBiO Technology (Shanghai) Corp., Ltd. The 293T cell line, supplied by the Chinese Academy of Sciences Cell Bank, was cultured at 37 °C in DMEM supplemented with 10% FBS under 5% CO_2. Before co-transfection, the cells were cultured in 96-well plates at 70% confluency for 24 h. For each well, firefly luciferase reporter plasmid (0.2 μg), Renilla luciferase internal control plasmid (0.01 μg), and microRNA (100 nM) were mixed with transfection reagent, incubated, and subsequently added to the cells. At 6 h post-transfection, the medium was substituted with fresh culture medium. The medium was removed at 48 h after transfection. Following washing with PBS, the cells were lysed with 1× Passive Lysis Buffer. The lysate supernatant was collected, and LAR II and Stop & Glo Reagent were sequentially added to a white 96-well plate. Renilla and firefly luciferase activities were estimated with a microplate reader (Infinite 200 PRO, Tecan, Männedorf, Switzerland) under light-protected conditions.

2.11. ROS Fluorescence Detection by the DCFH-DA Probe

ROS fluorescence detection was performed in preliminary, knockdown, and overexpression experiments. The experimental designs comprised three group configurations, specifically 7 groups (Control, PRV, PRV + DMSO, PRV + FNB25, PRV + FNB50, PRV + FNB100, and PRV + NAC); 3 groups (Control, si/oe-NC + PRV, and si/oe-Mir22hg + PRV or Control, si/oe-NC + PRV + FNB, and si/oe-Mir22hg + PRV + FNB); and 6 groups (Control, si/oe-NC + PRV/PRV + FNB, si/oe-Mir22hg + PRV/PRV + FNB, inhibitor/mimics-NC + PRV/PRV + FNB, inhibitor/mimics-miR362-2-5p + PRV/PRV + FNB, and si/oe-Mir22hg + inhibitor/mimics-miR362-2-5p + PRV/PRV + FNB).

RAW 264.7 cells were added to 48-well plates (cell density: 1.0×10^5 cells/mL) and cultured until they reached 80% confluency. Next, each treatment group was treated with PRV solution at an MOI of 1, while the Control group received DMEM; incubation continued for an additional 2 h. After washing, the Control group was replenished with 2% FBS-DMEM, and the various FNB treatment groups were supplemented with drug solutions, followed by further culturing for up to 12 h. After washing, the cells were incubated for 20 min with the DCFH-DA probe. Following the second washing cycle, observation and imaging were performed using a fluorescence microscope (excitation wavelength 488 nm, gain 1.4, exposure 400 ms).

2.12. Real-Time Quantitative PCR

The SPARKscript II All-in-one RT SuperMix Reverse Transcription Kit was used for RNA-to-cDNA reverse transcription. The reaction was carried out in a reaction system with a 20 μL volume comprising 0.4 μL each of upstream and downstream primers, cDNA (1.2 μL), nuclease-free H2O (8 μL), and 2× Universal SYBR Green qPCR Mix1 (10 μL). The amplification program was as follows: 1 cycle of 95 °C for 30 s; 40 cycles of 95 °C for 10 s, 60 °C for 10 s, and 72 °C for 20 s. The $2^{-\Delta\Delta Ct}$ method was employed for calculating the expression levels of the mRNAs of the target genes; β-actin served as the reference gene. Supplementary Materials provide details of the gene sequences.

2.13. Western Blotting (WB) Assay

The culture plate was filled with protease inhibitor-containing RIPA lysis buffer and incubated for 3–5 min. Using a cell scraper, we scraped and collected RAW 264.7 cells, which were lysed on ice for 30 min. Next, the mixture was centrifuged at 4 °C and 12,000 rpm for 10 min. The obtained supernatant constituted the total protein solution. This solution was mixed with 5× reducing protein loading buffer at a 4:1 ratio, denatured at 95 °C for 10 min in a metal bath, and preserved at −80 °C for subsequent analysis.

Next, SDS-PAGE was conducted on 10% separating and 5% concentrating gels. The separated proteins were electroblotted onto a PVDF membrane; subsequently, the membrane was blocked for 1 h using 5% skimmed milk. After incubating with specific primary antibodies, the membrane was prepared for color development with ultrasensitive ECL chemiluminescence. Grayscale values of the reference protein (β-actin) and target proteins were quantified by ImageJ software Version 1.54i. The ratio of grayscale values of the target protein and β-actin indicates the target protein's relative expression level.

2.14. In Vivo Experiments

SPF-grade KM mice (age: 7 weeks; weight: 20 ± 2 g) were utilized for in vivo experiments. The institutional animal ethics committee approved the experimental protocol (GXU-2023-0017). In both quarantine and experimental periods, water was provided ad libitum.

2.15. FNB Modulated Oxidative Stress in PRV-Infected Mice

Sixty SPF-grade KM mice (30 males and 30 females) were assigned to six groups (10 mice/group): Control, PRV, PRV + FNB25, PRV + FNB50, PRV + FNB100, and PRV + NAC. The Control group was administered a vehicle (no treatment). The PRV, FNB, and NAC groups were administered intramuscularly 0.2 mL PRV ($TCID_{50} = 10^{6.71}$/0.1 mL) on the first day of the experiment. Starting on the same day, FNB treatment group mice were administered FNB (25, 50, and 100 mg/kg body weight) once daily through the intragastric route until the animals were sacrificed. To determine the antioxidant capacity of FNB, all mice were sacrificed following PRV and FNB administration for 7 days.

2.16. Immunohistochemical (IHC) Analysis and Staining with Hematoxylin–Eosin (H&E)

Mouse lung sections were formalin-fixed, paraffin-embedded, and subjected to IHC analysis and H&E staining. After permeabilization with xylene and dehydration with ethanol, the sections underwent the antigen retrieval process using a citrate-based buffer. After quenching endogenous peroxidase activity with 3% H_2O_2, the sections were blocked with 2% BSA. Following overnight incubation of the sections with primary antibodies (iNOS, Nrf2, HO-1, and NQO1, 1:1000 dilution) at 4 °C and PBS washing, secondary antibodies (biotinylated rabbit IgG) were added. After rinsing with PBS, the sections underwent hematoxylin staining. After dehydration and mounting, the slides were viewed with a microscope at appropriate magnification.

2.17. Determination of ROS and NO Levels

Commercially available ROS and NO detection kits (Beyotime, Shanghai, China) were employed for estimating ROS and NO levels in RAW 264.7 cells. The DCFH-DA fluorescent probe assay was performed to determine intracellular ROS levels. The fluorescence intensity was measured after incubation in the dark and PBS washing (excitation/emission: 488/525 nm). NO content in supernatants was quantified by the Griess colorimetric method, with absorbance measured at 550 nm. All operations strictly followed the instructions of the corresponding detection kits. To ensure statistical accuracy, all experiments were independently repeated three times.

2.18. Statistical Analysis

Data analysis was performed with SPSS version 23.0 (IBM). Mean ± standard deviation (SD) was used to express the results. One-way analysis of variance together with Duncan's Multiple Range Test was utilized for multiple-group comparison. All experiments were repeated at least three times. For statistical comparison, groups having the same superscript letter showed no significant difference ($p > 0.05$), while groups with varying letters exhibited a significant difference ($p < 0.05$).

3. Results

3.1. Flavonoid-Targeted Metabolomics Elucidates the Monomeric Flavonoid Components in FNB

As shown in Table 1, flavonoid-targeted metabolomics detected monomeric flavonoid components in FNB, including hyperoside, quercetin dihydrate, isorhamnetin-3-O-glucoside, astragalin, kaempferol 3-O-β-D-galactopyranoside, quercetin, quercitrin, 3-O-methylquercetin, nepetin, taxifolin, kaempferol, and rutin. The contents of hyperoside, quercetin dihydrate, quercitrin, kaempferol 3-O-β-D-galactopyranoside, astragalin, isorhamnetin-3-O-glucoside, and quercetin exceeded 100 ng/mg. The complete results of the flavonoid-targeted metabolomics analysis are provided in Supplementary Materials.

Table 1. Identification of FNB components (content is denoted as mean ± SD, $n = 3$).

Flavonoid Type	Content (ng/mg of FNB)
Hyperoside	209.0820 ± 122.5221
Quercetin dihydrate	173.7680 ± 8.5066
Quercitrin	168.0843 ± 70.2847
Astragalin	152.7440 ± 62.0581
Isorhamnetin-3-O-glucoside	151.9935 ± 88.6834
Kaempferol 3-O-β-D-galactopyranoside	150.1312 ± 57.7227
Quercetin	132.4184 ± 5.1581
3-O-Methylquercetin	28.1981 ± 3.1799
Nepetin	27.8265 ± 4.7370
Taxifolin	20.6829 ± 9.8395
Kaempferol	16.8693 ± 7.7526
Rutin	13.7944 ± 3.5028
Rutin hydrate	13.7162 ± 3.4830
Schaftoside	13.3625 ± 3.9425

3.2. FNB Affects Oxidative Stress Due to PRV Infection in RAW 264.7 Cells

In the PRV group, ROS and NO levels were remarkably elevated, with substantial upregulation and downregulation of iNOS and NQO1, respectively ($p < 0.05$; Figure 1). However, in the low-, moderate-, and high-dose FNB groups, ROS and NO levels were significantly reduced; iNOS protein expression was significantly downregulated; and Nrf2, HO-1, and NQO1 protein expression levels were significantly upregulated ($p < 0.05$). Thus, FNB may modulate oxidative stress due to PRV infection by reducing excessive ROS and NO production and increasing antioxidant enzyme expression. To elucidate the specific molecular mechanism, RNA-seq was performed on PRV-infected RAW 264.7 cells treated with FNB.

3.3. Differential Expression of mRNAs, miRNAs, and lncRNAs

The principal component analysis (PCA) results of RNA-seq are shown in Figure 2A. The sample points for the Control, PRV, and PRV_FNB groups were closely clustered, indicating good reproducibility among the samples. The three groups were located in three distinct quadrants, suggesting remarkable differences among them in terms of RNA expression. The differential expression profiles of mRNAs, lncRNAs, and miRNAs are displayed in Figure 2B–D. Using the criteria (fold change > 2, $p < 0.05$), basic differential analysis was performed on the DE mRNAs, lncRNAs, and miRNAs from the RNA-seq data. Compared to the Control group, the PRV group had 1862 mRNAs differentially upregulated and 1687 mRNAs differentially downregulated; 685 lncRNAs differentially upregulated and 578 lncRNAs differentially downregulated; and 47 miRNAs differentially upregulated and 15 miRNAs differentially downregulated. Compared to the PRV group, the PRV_FNB group had 632 mRNAs differentially upregulated and 795 mRNAs differentially downregulated; 201 lncRNAs differentially upregulated and 259 lncRNAs differentially downregulated; and 5 miRNAs differentially upregulated and 6 miRNAs differentially downregulated.

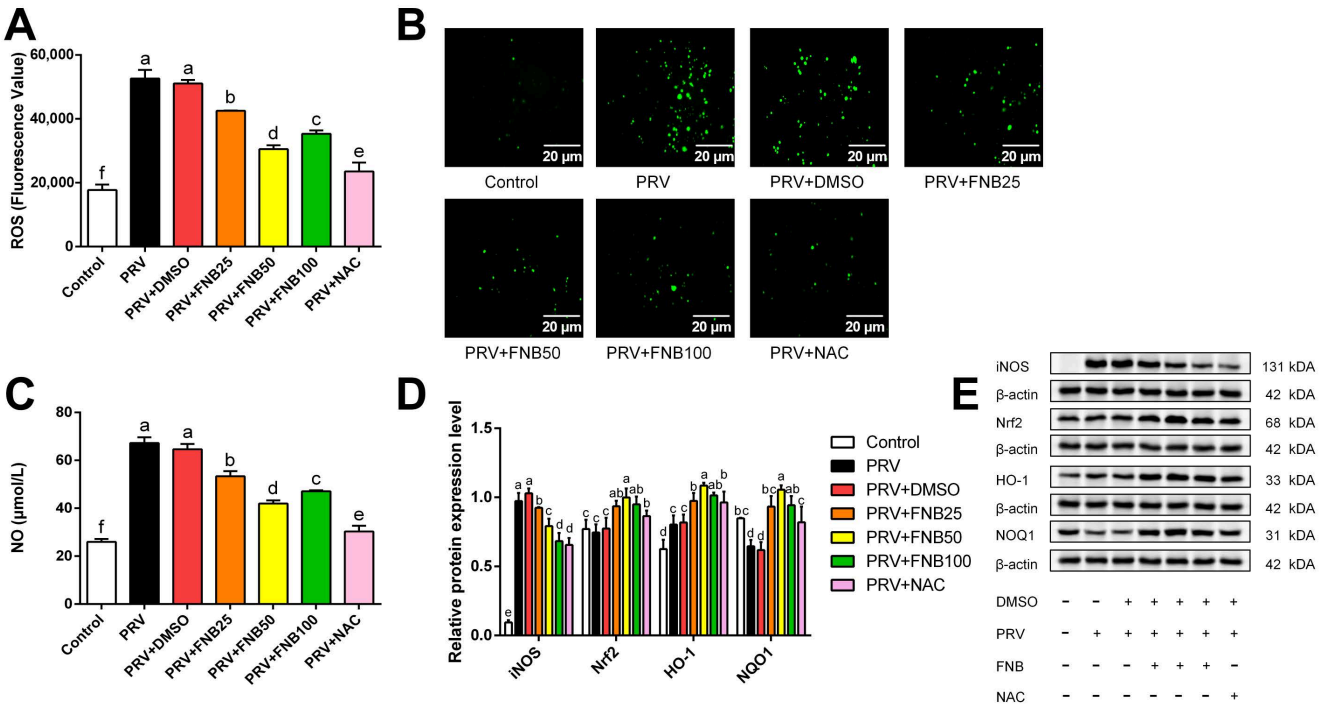


Figure 1. FNB modulates oxidative stress generated following PRV infection in RAW 264.7 cells ($n = 3$): (**A**) ROS levels. (**B**) ROS fluorescence observed under a fluorescence microscope. Green fluorescence indicates ROS-positive signals. (**C**) NO levels. (**D**) Quantitative analysis of iNOS, Nrf2, HO-1, and NQO1 protein expression levels. (**E**) WB bands of iNOS, Nrf2, HO-1, and NQO1. Bars with the same and varying letters above them imply a nonsignificant difference ($p > 0.05$) and a significant difference ($p < 0.05$), respectively. The same applies below.

3.4. GO Functional Enrichment Analysis for DE mRNAs

GO functional enrichment analysis was conducted to compare the Control and PRV groups for their DE mRNAs' functional roles. We focused on the upregulated DE mRNAs (Figure 3A). For the biological process category, the DE mRNAs were significantly enriched in the immune system process, defense response to virus, inflammatory response, innate immune response, immune response, cellular response to interferon-beta, negative regulation of viral genome replication, and response to virus. For the cellular component category, the DE mRNAs were significantly enriched in the cytosol, cytoplasm, endoplasmic reticulum, and perinuclear region of the cytoplasm, indicating their subcellular localization. For the molecular function category, the DE mRNAs were significantly enriched in protein binding, cytokine activity, MHC class I protein binding, and cytokine receptor activity.

We also focused on the downregulated mRNAs between the PRV and PRV_FNB groups (Figure 3D). For the biological process category, the DE mRNAs displayed substantial enrichment in inflammatory response, immune response, cellular response to interferon-beta, immune system process, defense response to virus, negative regulation of viral genome replication, innate immune response, and cellular response to interferon-gamma. For the cellular component category, the DE mRNAs showed remarkable enrichment in the extracellular region, plasma membrane, membrane, and cell surface, indicating their subcellular localization. In the molecular function category, the DE mRNAs were remarkably enriched in chemokine receptor activity, cytokine activity, chemokine activity, and signal transducer activity.

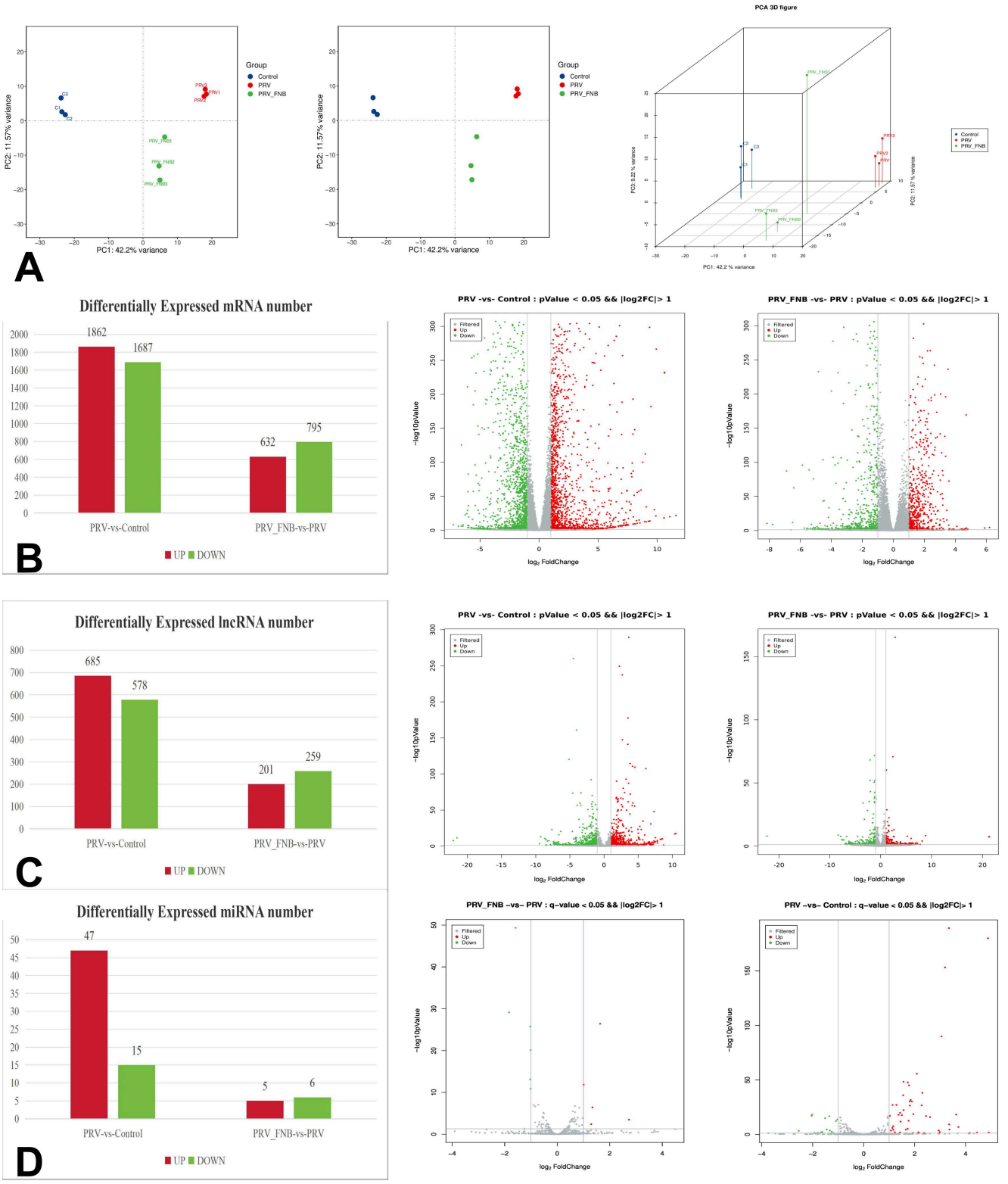


Figure 2. Differential expression patterns of lncRNAs, miRNAs, and mRNAs ($n = 3$): (**A**) PCA plot of RNA-seq samples. (**B**) Histogram and volcano plot of DE mRNAs. Red, green, and gray dots represent genes with differential upregulation, genes with differential downregulation, and non-differentially filtered genes, respectively. The same applies below. (**C**) Histogram and volcano plot of DE lncRNAs. (**D**) Histogram and volcano plot of DE miRNAs.

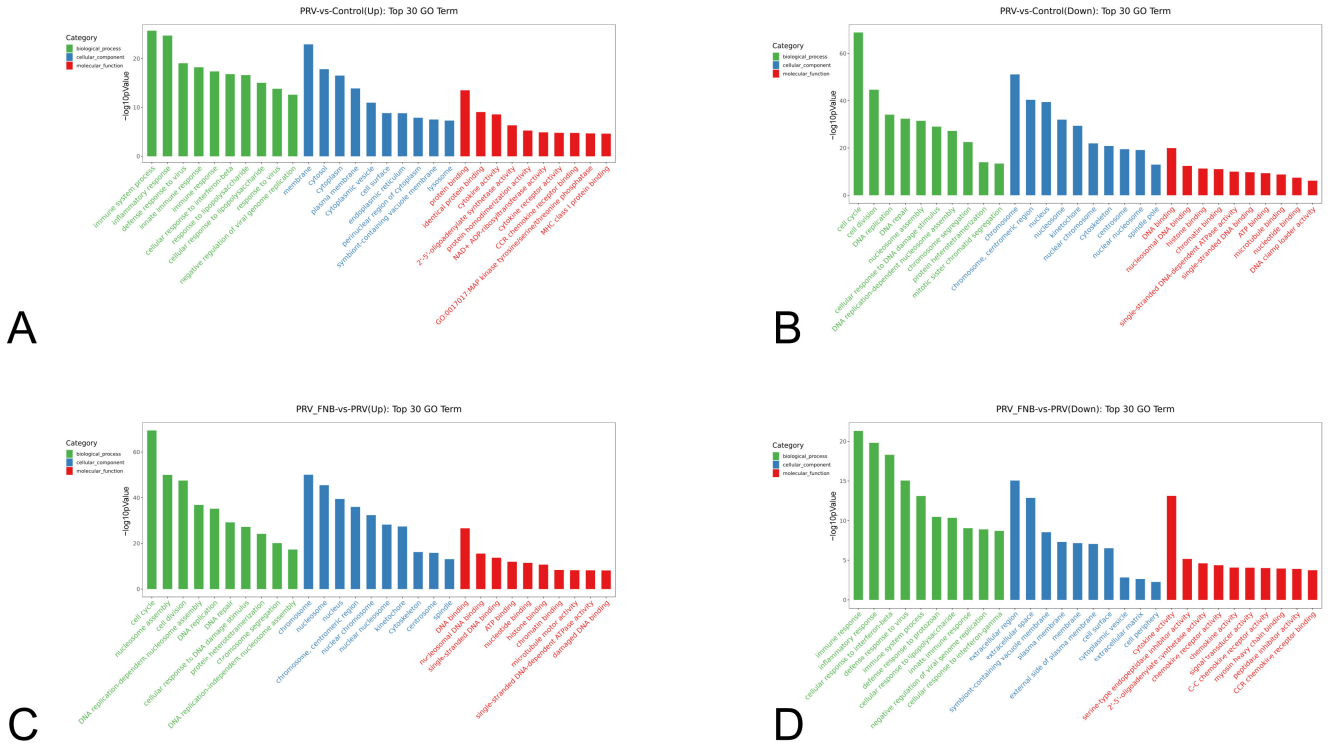


Figure 3. GO functional enrichment analysis of DE mRNAs ($n = 3$): (**A**,**B**) GO functional enrichment of differentially upregulated and differentially downregulated mRNAs between the Control and PRV groups. (**C**,**D**) GO functional enrichment of differentially upregulated and differentially downregulated mRNAs between the PRV_FNB and PRV groups.

3.5. KEGG Pathway Enrichment Analysis of DE mRNAs

To comprehend differences between the Control and PRV groups in terms of their DE mRNAs' functional roles, KEGG pathway enrichment analysis was conducted specifically for differentially upregulated mRNAs (Figure 4A). These mRNAs were predominantly enriched in the following signaling pathways: IL-17, TNF, Jak-STAT, Toll-like receptors, and NF-κB.

The downregulated mRNAs between the PRV and PRV_FNB groups were predominantly enriched in the following signaling pathways: IL-17, TNF, Toll-like receptors, and NF-κB.

3.6. Construction of the Mir22hg/miR-365-2-5p/iNOS Regulatory Axis

According to KEGG pathway enrichment analysis results, we performed cluster heatmap analysis on the DE mRNAs in the NF-κB signaling pathway (Figure 5A,B) and further screened ceRNAs according to targeting relationships by incorporating opposite expression trends and sequence complementarity scores. The results showed that all genes in this pathway were DEGs, and a ceRNA regulatory axis of *Mir22hg*/*miR-365-2-5p*-*iNOS* was identified (Figure 5C,D).

3.7. Validation of the Mir22hg/miR-365-2-5p/iNOS Regulatory Axis

To further validate the *Mir22hg*/*miR-365-2-5p*/*iNOS* regulatory axis (Figure 6A), we predicted the binding sites of *miR-365-2-5p* with *iNOS* as well as those of *Mir22hg* with *miR-365-2-5p* by using miRanda. Subsequently, we performed validation through dual-luciferase reporter assays. As shown in Figure 6B, *miR-365-2-5p* significantly reduced the luciferase activity of *iNOS*-WT ($p < 0.05$) but did not influence that of *iNOS*-MUT ($p > 0.05$). Similarly, *miR-365-2-5p* markedly reduced the luciferase activity of *Mir22hg*-WT ($p < 0.05$)

but did not influence that of *Mir22hg*-MUT ($p > 0.05$). Furthermore, as shown in Figure 6C, FISH results indicated that *Mir22hg* is localized in the cytoplasm, suggesting its potential biological role as a ceRNA through the corresponding molecular mechanism.

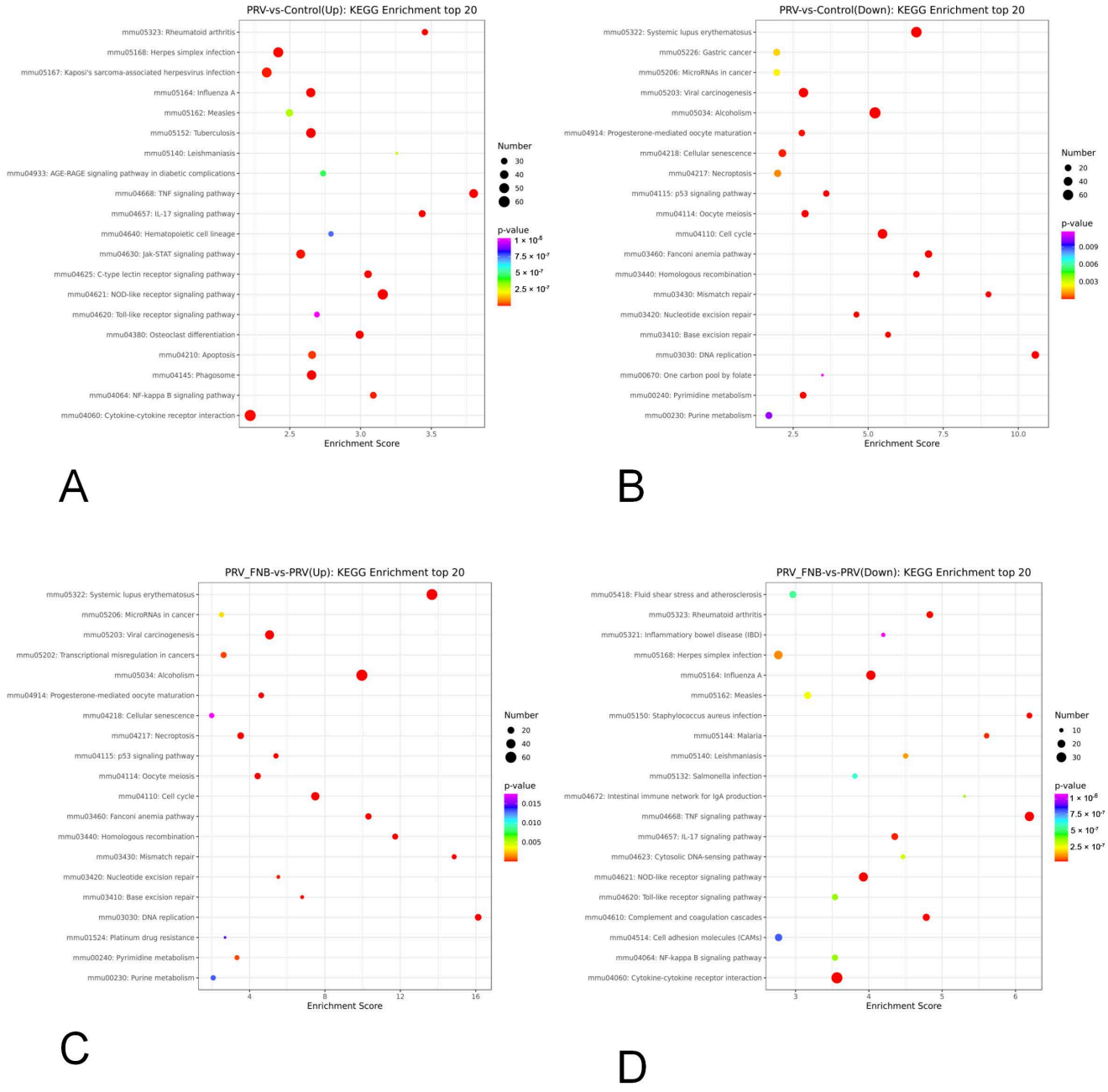


Figure 4. KEGG pathway enrichment analysis of DE mRNAs ($n = 3$): (**A**,**B**) KEGG pathway enrichment analysis of differentially upregulated and differentially downregulated mRNAs between the Control and PRV groups. (**C**,**D**) KEGG pathway enrichment analysis of differentially upregulated and differentially downregulated mRNAs between the PRV_FNB and PRV groups.

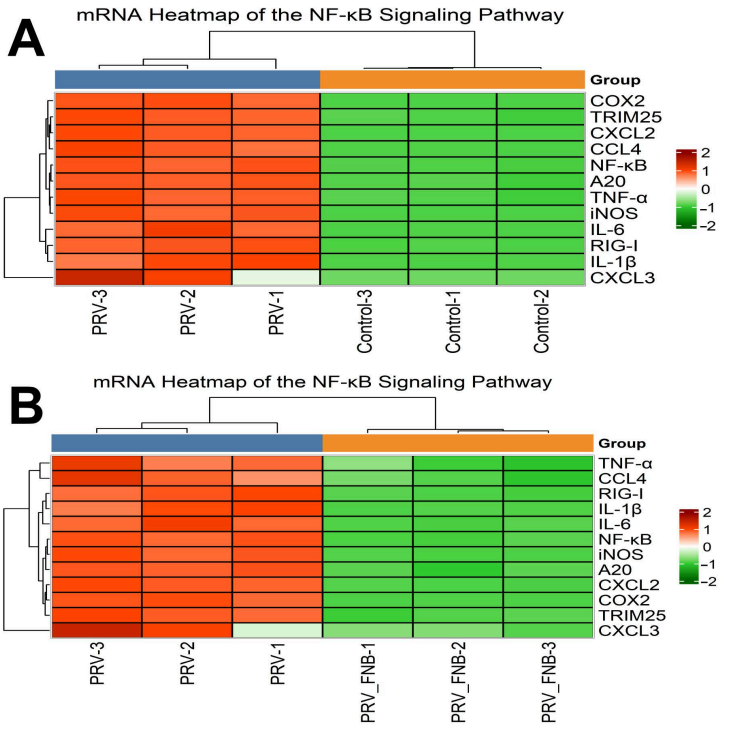


Figure 5. Construction of the *Mir22hg*/*miR-365-2-5p*/*iNOS* regulatory axis ($n = 3$): (**A**,**B**) The mRNA heatmap of the NF-κB signaling pathway. (**C**,**D**) A ceRNA regulatory axis of *Mir22hg*/*miR-365-2-5p*/*iNOS*. Red and green represent upregulated and downregulated expression of genes, respectively.

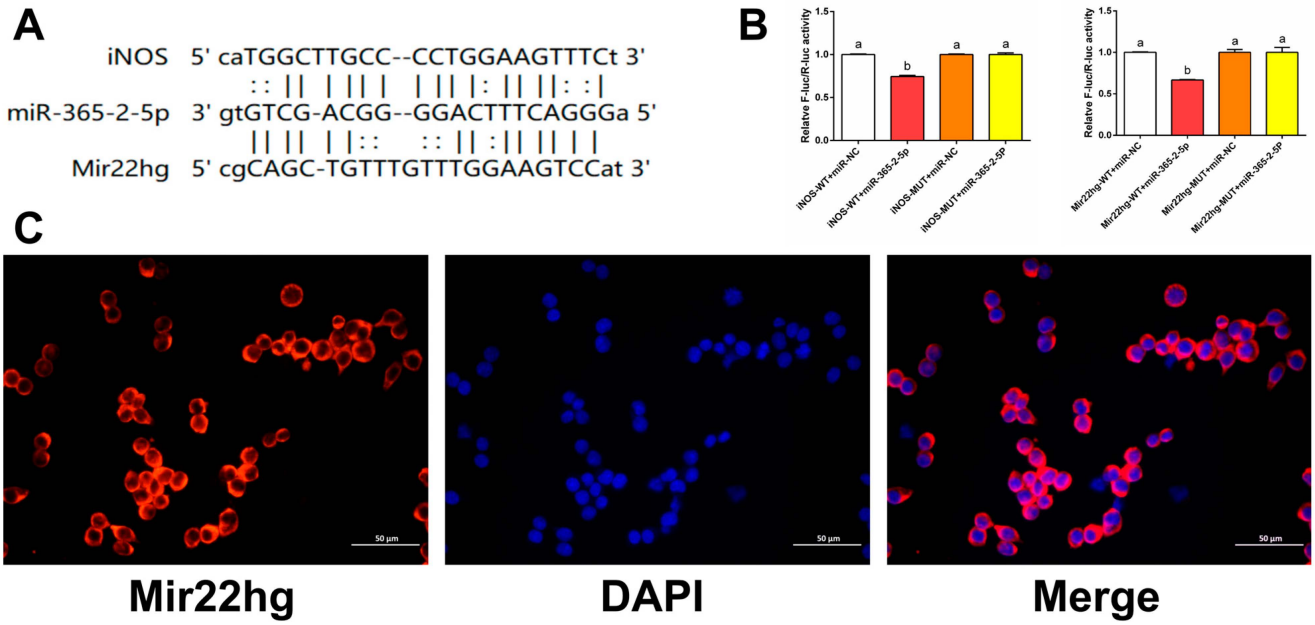


Figure 6. Validation of the *Mir22hg*/*miR-365-2-5p*/*iNOS* regulatory axis ($n = 3$): (**A**) *miR-365-2-5p* and *iNOS* binding sites; *Mir22hg* and *miR-365-2-5p* binding sites. (**B**) Dual-luciferase reporter experiment bar chart. (**C**) Subcellular localization of *Mir22hg*. The *Mir22hg* probe was stained red, and the nucleus was stained blue with DAPI; the red and blue signals did not overlap, indicating cytoplasmic localization of *Mir22hg*. Bars with the same letters above them indicate no significant difference ($p > 0.05$), while those with different letters indicate a significant difference ($p < 0.05$).

3.8. Mir22hg Function in RAW 264.7 Cells Following PRV Infection

We conducted functional studies on *Mir22hg*. In RAW264.7 cells with PRV infection, *Mir22hg* was knocked down by transfecting siRNAs targeting it. As shown in Figure 7A,

transfection with si-lnc-Mir22hg-2 significantly decreased *Mir22hg* expression ($p < 0.05$) and yielded optimal efficiency; therefore, subsequent experiments achieved *Mir22hg* knockdown by transfecting si-lnc-Mir22hg-2. Furthermore, *Mir22hg* knockdown remarkably attenuated ROS and NO levels in PRV-infected RAW264.7 cells (Figure 7B–D; $p < 0.05$). *Mir22hg* knockdown also significantly decreased *iNOS* mRNA and iNOS protein expression ($p < 0.05$) and significantly upregulated *miR-365-2-5p*, *HO-1*, *NQO1*, and *Nrf2* mRNA and HO-1, NQO1, and Nrf2 protein expression ($p < 0.05$) (Figure 7E–G).

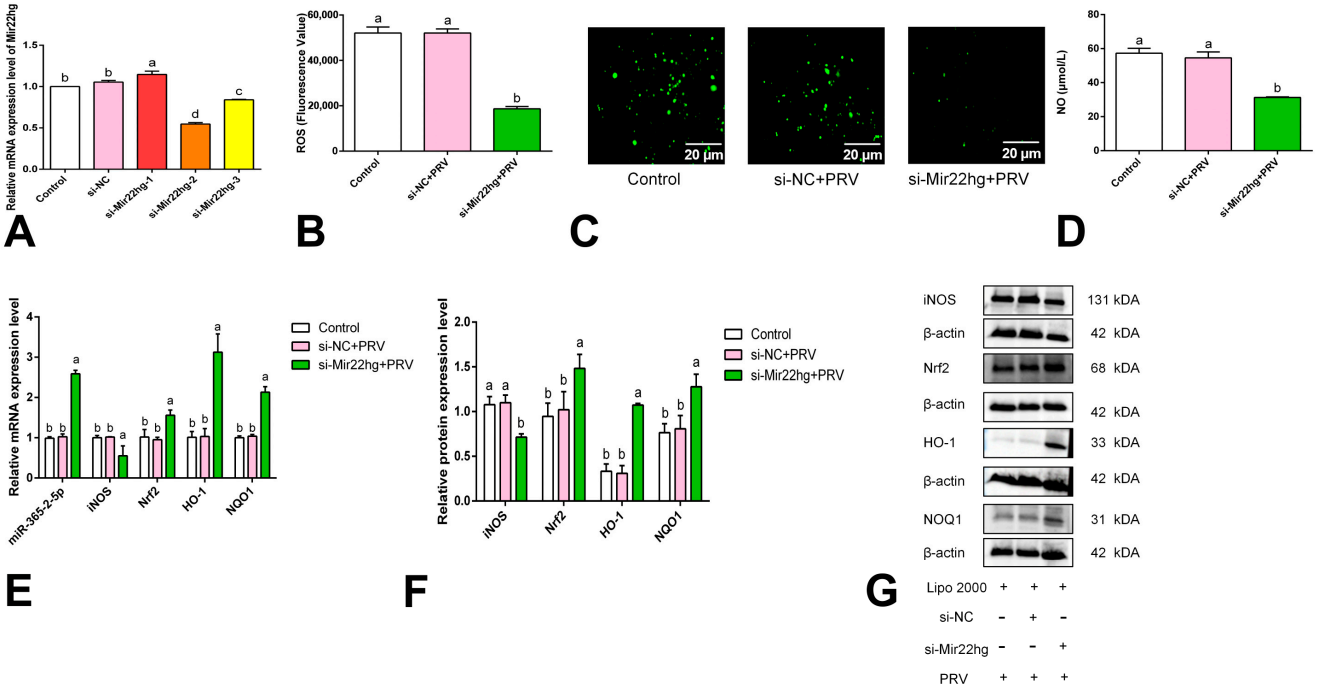


Figure 7. *Mir22hg* function in PRV-infected RAW 264.7 cells ($n = 3$): (**A**) Screening of siRNAs targeting *Mir22hg*. (**B**) Effect of *Mir22hg* knockdown on ROS levels in RAW 264.7 cells after PRV infection. (**C**) ROS fluorescence observed under a fluorescence microscope. Green fluorescence indicates ROS-positive signals. (**D**) Influence of *Mir22hg* knockdown on NO levels in PRV-infected RAW 264.7 cells. (**E**) Effect of *Mir22hg* knockdown on *miR-365-2-5p*, *iNOS*, *Nrf2*, *HO-1*, and *NQO1* mRNA expression. (**F**) Effect of *Mir22hg* knockdown on iNOS, HO-1, NQO1, and Nrf2 protein expression. (**G**) WB bands of iNOS, HO-1, NQO1, and Nrf2. Bars with the same letters above them indicate no significant difference ($p > 0.05$), while those with different letters indicate a significant difference ($p < 0.05$).

3.9. Mir22hg Function in FNB-Treated PRV-Infected RAW 264.7 Cells

To further complete the functional investigation of *Mir22hg*, we overexpressed it in FNB-treated RAW264.7 cells infected with PRV by transfecting a plasmid containing its sequence. Interestingly, we observed results opposite to those obtained with its knockdown. As shown in Figure 8A–C, *Mir22hg* overexpression in these cells significantly increased NO and ROS levels ($p < 0.05$). As shown in Figure 8D–F, *Mir22hg* overexpression also significantly elevated the expression of *iNOS* mRNA and iNOS protein ($p < 0.05$) and markedly reduced *miR-365-2-5p*, *HO-1*, *NQO1*, and *Nrf2* mRNA and protein expression ($p < 0.05$).

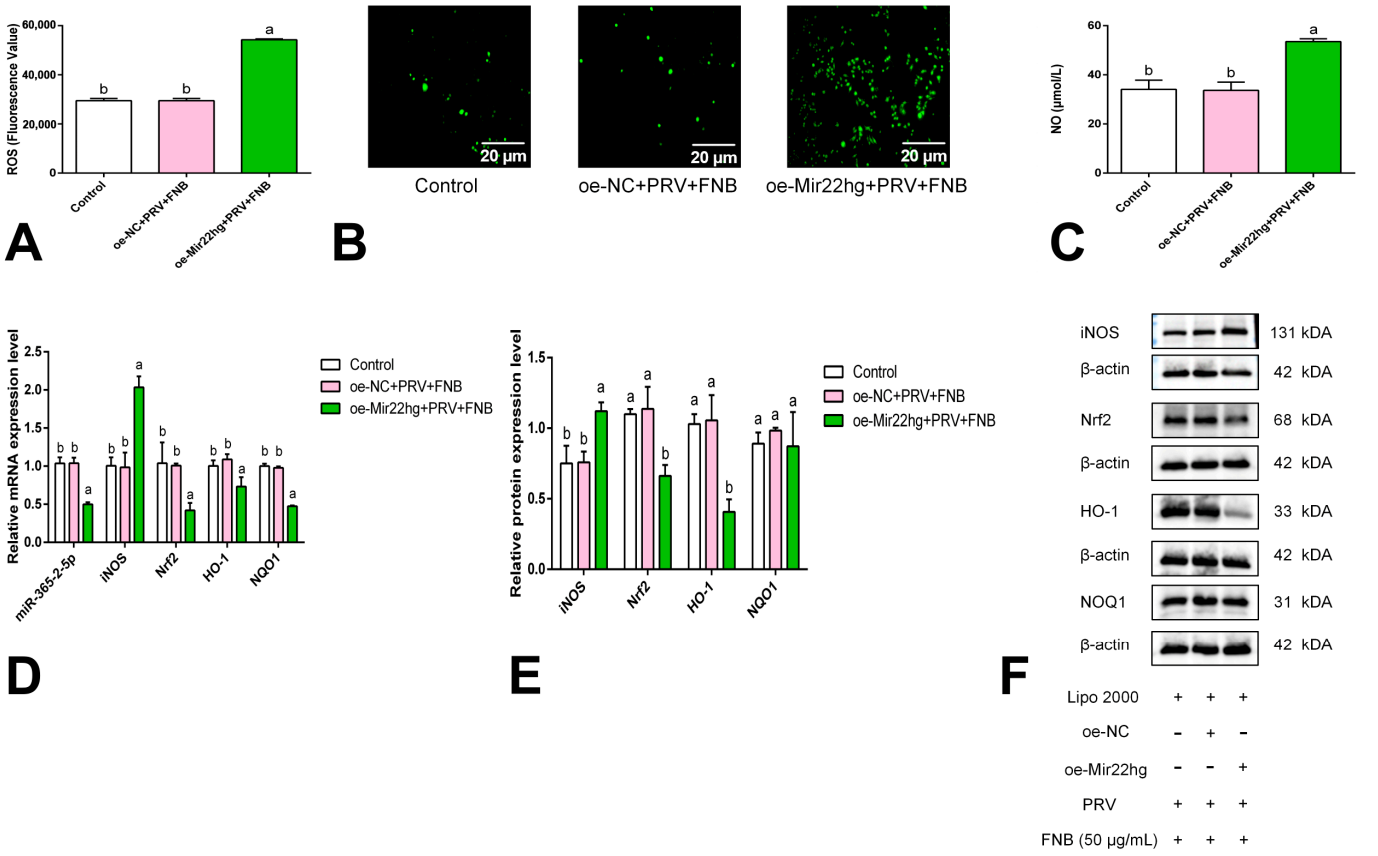


Figure 8. Role of *Mir22hg* in FNB-treated, PRV-infected RAW 264.7 cells ($n = 3$): (**A**) Influence of *Mir22hg* overexpression on ROS levels in FNB-treated, PRV-infected RAW 264.7 cells. (**B**) ROS fluorescence observed under a fluorescence microscope. Green fluorescence indicates ROS-positive signals. (**C**) Effect of *Mir22hg* overexpression on NO levels in FNB-treated, PRV-infected RAW 264.7 cells. (**D**) Influence of *Mir22hg* overexpression on *miR-365-2-5p*, *iNOS*, *Nrf2*, *HO-1*, and *NQO1* mRNA expression. (**E**) Effect of *Mir22hg* overexpression on iNOS, NQO1, Nrf2, and HO-1 protein expression levels. (**F**) WB bands of iNOS, NQO1, Nrf2, and HO-1. Bars with the same letters above them indicate no significant difference ($p > 0.05$), while those with different letters indicate a significant difference ($p < 0.05$).

3.10. The Mir22hg/miR-365-2-5p/iNOS Axis Mediates Oxidative Stress Modulation in PRV-Infected RAW 264.7 Cells

Rescue experiments were conducted to examine the *Mir22hg*/*miR-365-2-5p*/*iNOS* axis's role in influencing oxidative stress in PRV-infected RAW 264.7 cells. As shown in Figure 9A–F, in RAW 264.7 cells with PRV infection, *miR-365-2-5p* knockdown significantly increased ROS and NO levels, significantly upregulated the expression of *iNOS* mRNA and iNOS protein, and remarkably decreased NQO1, Nrf2, and HO-1 mRNA and NOQ1, Nrf2, and HO-1 protein expression ($p < 0.05$). However, co-knockdown of *Mir22hg* reversed the aggravated oxidative stress caused by *miR-365-2-5p* knockdown.

As shown in Figure 9G–L, *miR-365-2-5p* overexpression significantly decreased ROS and NO levels, significantly downregulated the expression of *iNOS* mRNA and iNOS protein, and substantially improved *HO-1*, *NQO1*, and *Nrf2* mRNA and HO-1, NQO1, and Nrf2 protein expression ($p < 0.05$). However, co-overexpression of *Mir22hg* reversed the enhanced antioxidant capacity induced by *miR-365-2-5p* overexpression.

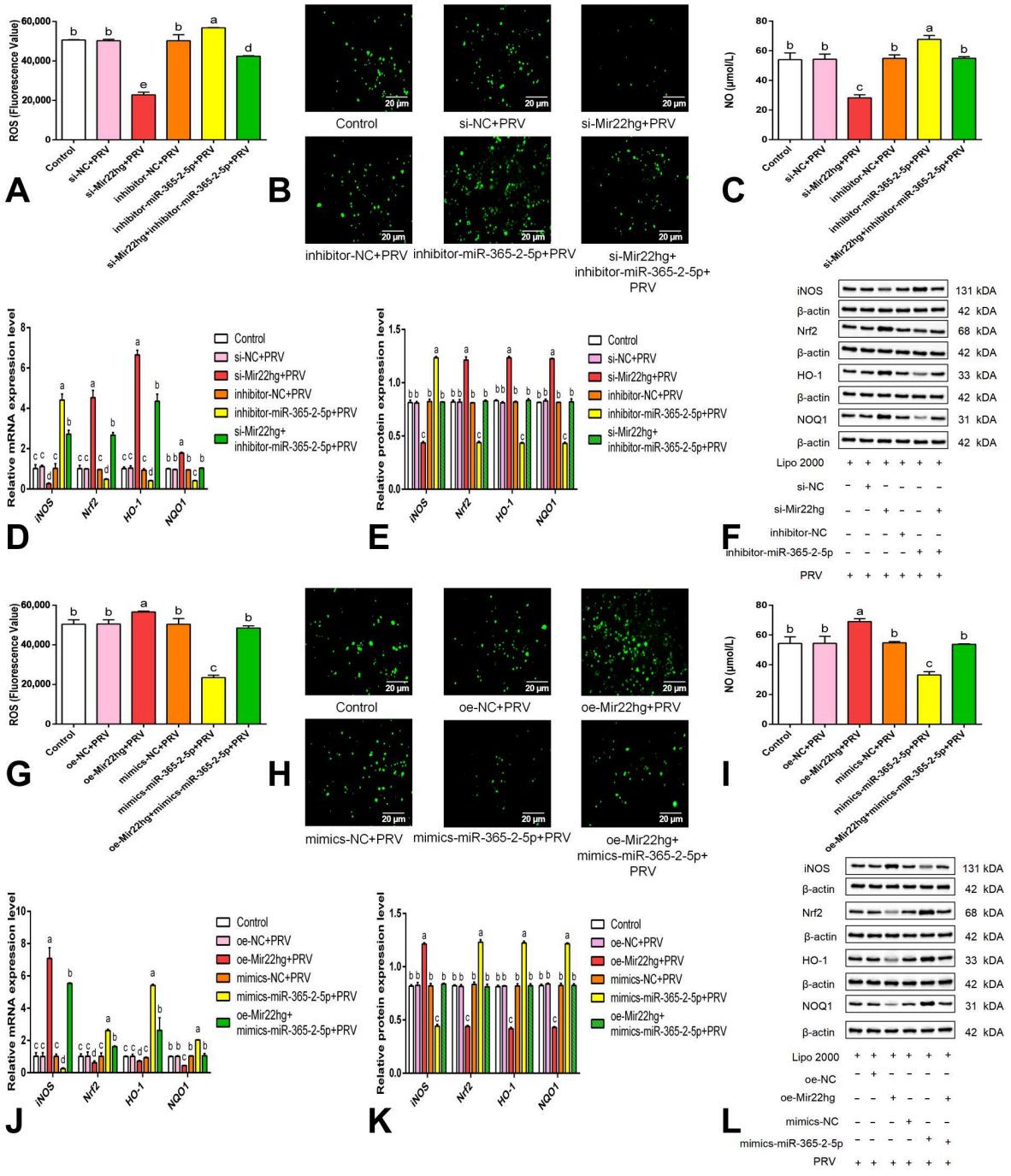


Figure 9. Effect of the *Mir22hg*/*miR-365-2-5p*/*iNOS* axis on oxidative stress in RAW 264.7 cells with PRV infection ($n = 3$): (**A**) Influence of *Mir22hg* and *miR-365-2-5p* knockdown on ROS levels in PRV-infected RAW 264.7 cells. (**B**) ROS fluorescence observed under a fluorescence microscope. Green fluorescence indicates ROS-positive signals. (**C**) Effect of *Mir22hg* and *miR-365-2-5p* knockdown on NO levels in PRV-infected RAW 264.7 cells. (**D**) Effect of *Mir22hg* and *miR-365-2-5p* knockdown on *iNOS*, *NQO1*, *Nrf2*, and *HO-1* mRNA expression. (**E**) Effect of *Mir22hg* and *miR-365-2-5p* knockdown on iNOS, Nrf2, HO-1, and NQO1 protein levels. (**F**) WB bands of iNOS, NQO1, Nrf2, and HO-1. (**G**) Effect of *Mir22hg* and *miR-365-2-5p* overexpression on ROS levels in PRV-infected RAW 264.7 cells. (**H**) ROS fluorescence observed under a fluorescence microscope. Green fluorescence indicates ROS-positive signals. (**I**) Effect of *Mir22hg* and *miR-365-2-5p* overexpression on NO levels in PRV-infected RAW 264.7 cells. (**J**) Effect of *Mir22hg* and *miR-365-2-5p* overexpression on *iNOS*, *Nrf2*, *HO-1*, and *NQO1* mRNA expression. (**K**) Effect of *Mir22hg* and *miR-365-2-5p* overexpression on iNOS, NQO1, Nrf2, and HO-1 protein expression. (**L**) WB bands of iNOS, Nrf2, HO-1, and NQO1. Bars with the

same letters above them indicate no significant difference ($p > 0.05$), while those with different letters indicate a significant difference ($p < 0.05$).

3.11. Effect of the Mir22hg/miR-365-2-5p/iNOS Axis on Oxidative Stress in FNB-Treated, PRV-Infected RAW 264.7 Cells

In FNB-treated, PRV-infected RAW264.7 cells, *miR-365-2-5p* knockdown significantly increased ROS and NO levels; significantly upregulated the expression of *iNOS* mRNA and iNOS protein; and significantly downregulated *NQO1*, *Nrf2*, and *HO-1* mRNA and NQO1, Nrf2, and HO-1 protein expression (Figure 10A–F, $p < 0.05$). However, co-knockdown of *Mir22hg* reversed the aggravated oxidative stress induced by *miR-365-2-5p* knockdown.

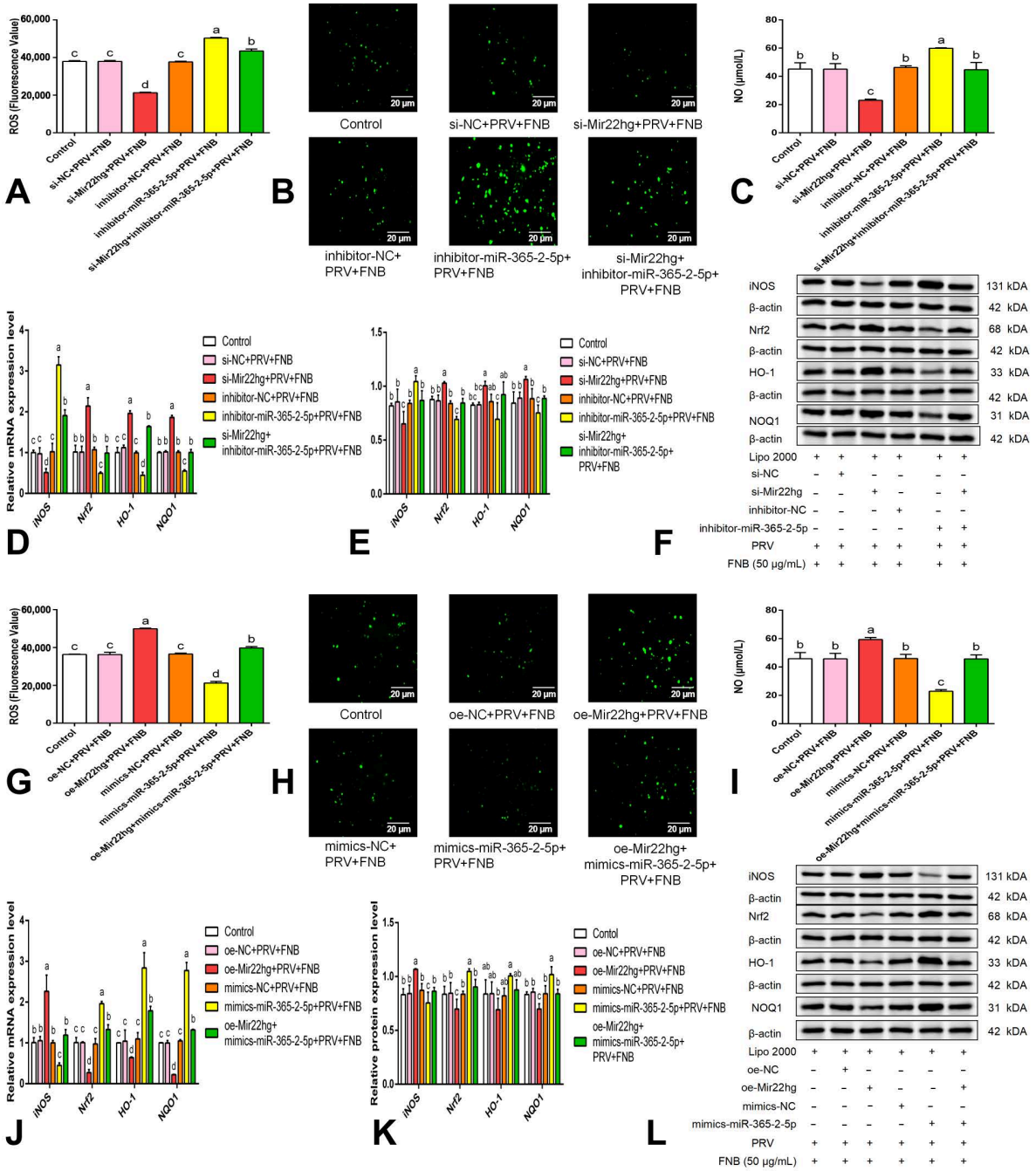


Figure 10. Influence of the *Mir22hg/miR-365-2-5p/iNOS* axis on oxidative stress in FNB-treated, PRV-infected RAW 264.7 cells ($n = 3$): (**A**) Effect of *Mir22hg* and *miR-365-2-5p* knockdown on ROS levels in FNB-treated, PRV-infected RAW 264.7 cells. (**B**) ROS fluorescence observed under a fluorescence

microscope. Green fluorescence indicates ROS-positive signals. (**C**) Effect of *Mir22hg* and *miR-365-2-5p* knockdown on NO levels in FNB-treated, PRV-infected RAW 264.7 cells. (**D**) Effect of *Mir22hg* and *miR-365-2-5p* knockdown on *iNOS*, *NQO1*, *Nrf2*, and *HO-1* mRNA expression. (**E**) Effect of *Mir22hg* and *miR-365-2-5p* knockdown on iNOS, HO-1, NQO1, and Nrf2 protein levels. (**F**) WB bands of iNOS, NQO1, Nrf2, and HO-1. (**G**) Effect of *Mir22hg* and *miR-365-2-5p* overexpression on ROS levels in FNB-treated, PRV-infected RAW 264.7 cells. (**H**) ROS fluorescence observed under a fluorescence microscope. Green fluorescence indicates ROS-positive signals. (**I**) Effect of *Mir22hg* and *miR-365-2-5p* overexpression on NO levels in FNB-treated, PRV-infected RAW 264.7 cells. (**J**) Effect of *Mir22hg* and *miR-365-2-5p* overexpression on *iNOS*, *NQO1*, *Nrf2*, and *HO-1* mRNA expression. (**K**) Effect of Mir22hg and miR-365-2-5p overexpression on iNOS, HO-1, NQO1, and Nrf2 protein levels. (**L**) WB bands of iNOS, NQO1, Nrf2, and HO-1. Bars with the same letters above them indicate no significant difference ($p > 0.05$), while those with different letters indicate a significant difference ($p < 0.05$).

As shown in Figure 10G–L, *miR-365-2-5p* overexpression significantly decreased ROS and NO levels, significantly downregulated the expression of *iNOS* mRNA and iNOS protein, and significantly upregulated *NQO1*, *Nrf2*, and *HO-1* mRNA and protein expression ($p < 0.05$). However, co-overexpression of *Mir22hg* reversed the enhanced antioxidant capacity resulting from *miR-365-2-5p* overexpression.

3.12. Effects of FNB on Regulating Oxidative Stress in PRV-Induced Model Mice

KM mice were intramuscularly injected with a single dose of PRV ($TCID_{50}$ = $10^{6.71}$/0.1 mL) on experiment day 1. Mice were also administered FNB (25, 50, and 100 mg/kg body weight) through daily oral gavage for 7 days (Figure 11A). H&E staining of lung tissue sections from mice in the PRV group revealed thickened alveolar walls and significant inflammatory cell infiltration within the alveolar spaces (Figure 11B). Compared to the PRV group, treatment with moderate and high doses of FNB restored normal alveolar structure, eliminated inflammatory cell infiltration, and alleviated the PRV infection-triggered inflammatory response. According to IHC analysis, the PRV group displayed significantly increased expression of iNOS protein ($p < 0.05$) and remarkably decreased NQO1, Nrf2, and HO-1 protein expression ($p < 0.05$) compared to the Control group. Following FNB treatment, the low-, moderate-, and high-dose FNB groups showed significantly reduced iNOS protein expression ($p < 0.05$) and markedly elevated NQO1, Nrf2, and HO-1 protein expression ($p < 0.05$). Notably, the increase in Nrf2 exhibited a dose-dependent trend (Figure 11C). Finally, q-PCR results, as shown in Figure 11D, indicated that PRV infection significantly upregulated *iNOS* mRNA expression and remarkably downregulated *NQO1*, *Nrf2*, and *HO-1* mRNA expression ($p < 0.05$). In contrast, moderate- and high-dose FNB treatments significantly reversed these effects ($p < 0.05$). Interestingly, in vivo, PRV infection also significantly upregulated *Mir22hg* expression and substantially reduced *miR-365-2-5p* expression ($p < 0.05$). Treatment with FNB at low, moderate, and high doses similarly and significantly downregulated *Mir22hg* expression and markedly elevated *miR-365-2-5p* expression ($p < 0.05$) dose-dependently.

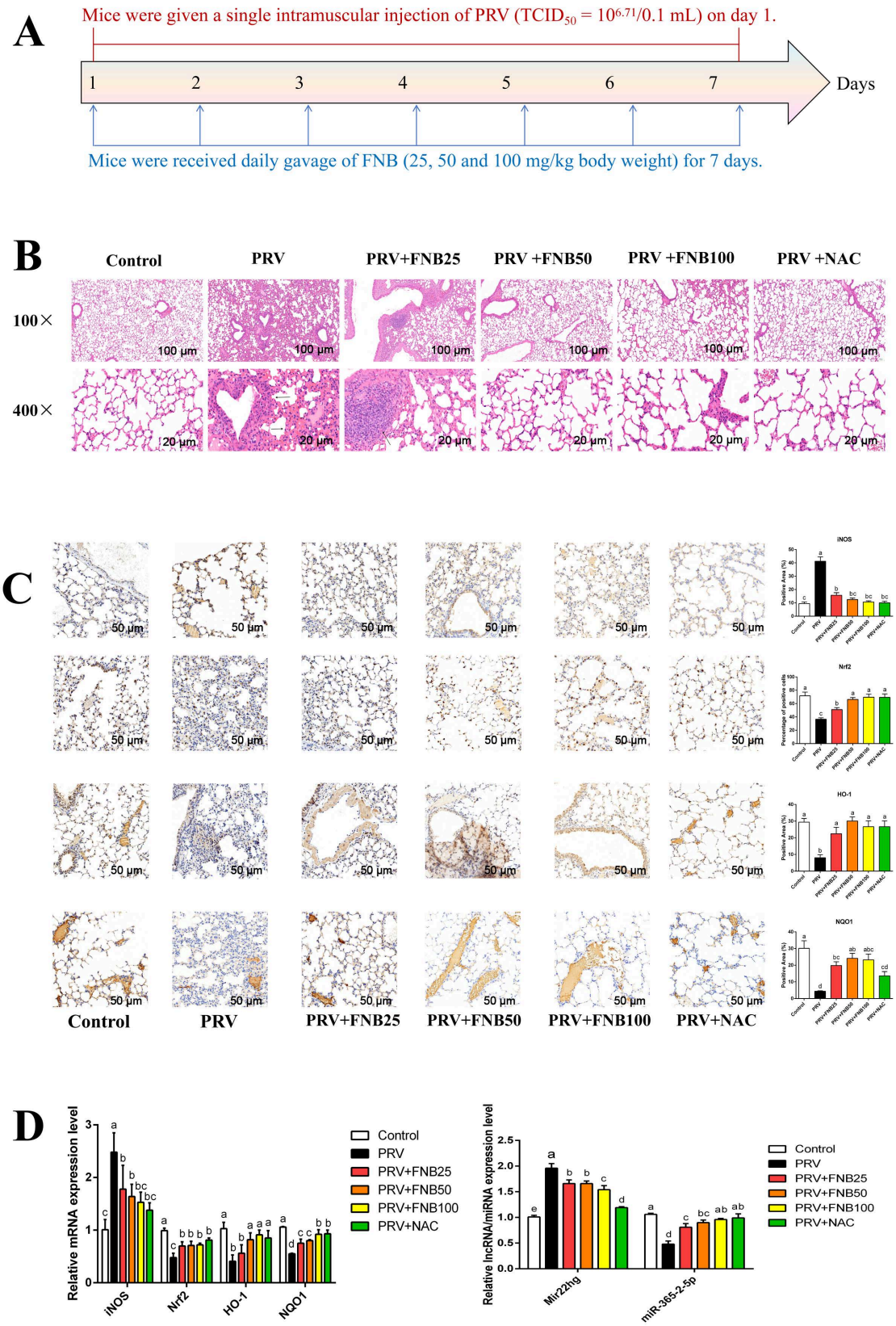


Figure 11. Effects of FNB on oxidative stress modulation in PRV-induced model mice (n = 10): (**A**) Schematic diagram of FNB treatment of the PRV-induced in vivo oxidative stress model. (**B**) HE-stained pathological sections of mouse lungs. (**C**) iNOS, NQO1, Nrf2, and HO-1 protein expression in mouse lungs. (**D**) *iNOS*, *NQO1*, *Nrf2*, *HO-1*, *Mir22hg*, and *miR-365-2-5p* mRNA expression in mouse lungs. Bars with the same letters above them indicate no significant difference ($p > 0.05$), while those with different letters indicate a significant difference ($p < 0.05$).

4. Discussion

Mounting evidence confirms the pivotal role of oxidative stress in viral pathogenesis. Zhao et al. [17] found that infection with PRV causes a surge in mitochondrial Ca^{2+} concentration, mitochondrial membrane potential loss, and excessive generation of ROS. Simultaneously, PRV infection sequesters Nrf2 in the cytoplasm, hindering its translocation into the nucleus to initiate antioxidant responses, thereby preventing the effective clearance of intracellular ROS. The sustained accumulation of ROS at high levels triggers mitophagy, which selectively removes damaged mitochondria and the mitochondrial antiviral signaling protein (MAVS) localized on their surface. This suppresses MAVS-mediated type I interferon responses, creating favorable conditions for PRV replication. Marcaccini et al. [18] showed that following PRV infection of the porcine nervous system, all potential NO sources are activated, leading to excessive NO production during infection with the neuroinvasive alphavirus PRV. Lin et al. [19] found that, in RAW 264.7 cells, PRV infection significantly upregulates protein expression of iNOS, markedly amplifies inflammatory cytokine production, and significantly downregulates Nrf2 and NQO1 protein expression, thereby inducing oxidative stress and inflammation development. Huan et al. [20] constructed a mouse model with PRV infection-induced oxidative stress and inflammation and observed inflammatory damage in the brain and lungs of infected mice, together with significantly elevated levels of ROS, MDA, and significantly decreased SOD activity. Consistent with these findings, the in vitro and in vivo experiments of the present study indicate that PRV infection significantly increases ROS, NO, and iNOS levels while significantly reducing Nrf2, HO-1, and NQO1 levels; these findings align with the results and observations of previous research.

The predominant phytochemical constituents of *P. hydropiper* L. are flavonoids, accounting for over 50% of its composition, and they exhibit potent antioxidant activity [21]. Bairagi et al. [22] isolated and identified 40 major flavonoid monomers from the flavonoids of *P. hydropiper* L. However, with the use of new targeted metabolomics technology, a large number of its monomeric components can be identified. In this study, based on an established standard library of 386 flavonoid monomers, targeted metabolomics technology was used to identify the flavonoid monomers and their contents in FNB. Ren et al. [23] demonstrated that the *P. hydropiper* L. ethyl acetate fraction of flavonoids (FEA) could significantly reduce ROS, NO, and iNOS levels; decrease NF-κB p65 nuclear translocation; and alleviate oxidative stress and inflammatory responses induced by PRV infection in RAW 264.7 cells. Similarly, a study by Chen et al. [24] showed that *Polygonum hydropiper* L. ethanol extract could activate Nrf2 signaling and upregulate glutathione (GSH) synthesis genes, significantly decrease the levels of MDA, LPO, and 4-HNE, but significantly increase the levels of CAT, SOD, and GSH, thereby attenuating oxidative stress and inflammatory responses. Interestingly, in the present study, both in vitro and in vivo experiments indicate that FNB can significantly reduce ROS, NO, and iNOS levels; significantly increase NQO1, Nrf2, and HO-1 levels; and affect PRV infection-induced oxidative stress. This aligns with the findings and results of previous studies. However, the molecular mechanisms specifically involved in these processes are unclear. Therefore, we subsequently conducted RNA-seq analysis.

RNA-seq revealed substantial alterations in the mRNA expression profile of RAW 264.7 cells following PRV infection. We identified 3549 DE mRNAs, 1263 DE lncRNAs, and 62 DE miRNAs. Treatment of PRV-infected RAW 264.7 cells with FNB further altered the mRNA expression profile, as indicated by 1427 DE mRNAs, 460 DE lncRNAs, and 11 DE miRNAs. These changes were analyzed using GO and KEGG analyses. Based on GO analysis, the DE mRNAs displayed substantial enrichment in the biological process terms—inflammatory response and antiviral response. According to KEGG analysis, the DE mRNAs displayed remarkable enrichment in the NF-κB pathway. Liu et al. [25] ob-

served that the flavonoid luteolin reduces excessive NO production through NF-κB/iNOS pathway suppression and attenuates oxidative stress and inflammatory responses induced by PRV infection in RAW 264.7 cells by inducing Nrf2-mediated HO-1 expression. Jiang et al. [26] showed that the flavonoid quercitrin affects oxidative stress due to PRV infection through Nrf2 signaling pathway activation, HO-1 and NQO1 expression elevation, and iNOS expression reduction. Our sequencing results align with their findings, confirming the NF-κB/iNOS/Nrf2/HO-1 pathway's essential role in PRV infection-induced oxidative stress and its modulation by flavonoids.

To elucidate the molecular mechanism through which FNB exerts its regulatory effects and to identify the ceRNA axis it controls, we utilized a three-pronged strategy. First, we screened 12 DE mRNAs from the KEGG-enriched NF-κB signaling pathway. Second, we utilized miRanda to predict the binding sites between miRNAs and mRNAs, as well as between lncRNAs and miRNAs. Finally, we constructed and confirmed the *Mir22hg*/*miR-365-2-5p*/*iNOS* ceRNA regulatory axis based on the results of dual-luciferase reporter assays and FISH experiments. As mentioned earlier, lncRNAs can prevent miRNA degradation or mRNA silencing by competitively binding to miRNAs, a mechanism mediating the biological effects of lncRNAs. Cao et al. [27] demonstrated that *Arthrospira platensis* polysaccharide may enhance PRV-infected RAW 264.7 cells' antioxidant ability by controlling the circRNA-miRNA-mRNA network and antioxidant-associated signaling pathways. Zhen et al. [28] showed that the flavonoid baicalin upregulates *miR-15a* expression, leading to the disruption of the ceRNA balance and downregulation of *CDC42*/*MAP3K1* expression, thereby causing JNK signaling pathway inhibition and suppression of oxidative stress and inflammation development. Our findings align with the observations of these authors. Salman et al. [29] also indicated that *Mir22hg*, β-catenin, and C-myc serum levels were downregulated in pancreatic cancer; serum *Mir22hg* and β-catenin were inversely correlated with distant metastasis; serum *Mir22hg* was identified as an independent predictor of pancreatic cancer; and *Mir22hg* may be regarded as a potential marker for pancreatic cancer. Wei et al. [30] found that in mouse keratinocytes, *miR-365-2-5p* attenuation elevated SIRT1 and FOXO1 protein expression, reduced the protein expression of STAT2, promoted the migration and growth of cells, and decreased the production of inflammatory factors, thus showing critical involvement in the mouse skin wound healing process and offering a new wound healing target. In the present study, FNB upregulated *miR-365-2-5p* expression and downregulated *Mir22hg* and iNOS expression, thereby reversing the PRV infection-induced downregulation of NQO1, Nrf2, and HO-1 and preventing oxidative stress progression in RAW 264.7 cells. Our results thus clarify the hitherto unknown roles of *Mir22hg* and *miR-365-2-5p* in the viral infection process and the regulatory effect of flavonoids on them.

NO produced by highly active iNOS can cause stress and damage to cells and tissues. In addition to enhancing oxygen free radical production through several mechanisms, its derivatives also disrupt the function of key antioxidant enzymes such as NQO1, Nrf2, and HO-1, further resulting in intracellular ROS accumulation [31]. Kang et al. [32] demonstrated that quercetin can reduce oxidative stress by inhibiting iNOS activity and inducing HO-1 expression mediated by Nrf2. The present study identified iNOS as a downstream target of *miR-365-2-5p*. RNA-seq showed that *iNOS* and *Mir22hg* were markedly upregulated and *miR-365-2-5p* was significantly downregulated in the PRV group compared to those in the Control group; furthermore, the PRV_FNB group showed significant downregulation of *iNOS* and *Mir22hg* and significant upregulation of *miR-365-2-5p* compared to the PRV group. We further validated the ceRNA regulatory mechanism in subsequent experiments. The results indicate that following PRV infection, *Mir22hg* competitively binds to *miR-365-2-5* in RAW 264.7 cells and upregulates *iNOS* expression, highlighting *Mir22hg*'s pivotal function in PRV infection progression. Interestingly, functional rescue experiments revealed that

miR-365-2-5p knockdown enhanced the inhibitory effects of *iNOS* and *Mir22hg* on the Nrf2 signaling pathway, which eventually increased excessive ROS and NO production. However, *miR-365-2-5p* overexpression reversed the inhibitory effects of *iNOS* and *Mir22hg* on the Nrf2 signaling pathway and reduced excessive ROS and NO production. Identical results were observed for RAW 264.7 cells infected with PRV and RAW 264.7 cells infected with PRV and treated with FNB. Thus, FNB modulates oxidative stress generated by PRV infection in RAW 264.7 cells through the *Mir22hg*/*miR-365-2-5p*/*iNOS* ceRNA regulatory axis.

In the functional experiments of *Mir22hg* (Figures 7 and 8), the exogenous *Mir22hg* plasmid is driven by the strong CMV promoter, which produces extremely high transcriptional levels and is not subject to the transcriptional regulation of endogenous genes by FNB. FNB can downregulate endogenous *Mir22hg*, yet it cannot inhibit the plasmid promoter or rapidly degrade the excessively accumulated *Mir22hg* transcripts. For this reason, FNB cannot reverse the phenotype induced by forced overexpression. Artificial forced overexpression serves as an extreme strategy for functional validation. Under the physiological state of genuine viral infection, *Mir22hg* expression is fully controlled by endogenous signaling pathways. In this scenario, FNB efficiently downregulates endogenous *Mir22hg*, as confirmed by RNA-seq and mouse in vivo experiments.

Despite these supportive findings, several limitations of the present study should be acknowledged. This study is predominantly based on in vitro experiments using RAW264.7 cells. Although a mouse model was included, we did not perform in vivo knockdown or overexpression targeting this ceRNA axis directly. Future validation of this mechanism could be conducted in porcine alveolar macrophage cell lines, primary cells, or conditional knockout mice. In addition, the screening scope for the ceRNA network in our work is limited: we mainly focused on differentially expressed mRNAs within the NF-κB pathway, while other oxidative stress-related pathways and alternative ceRNA axes were not systematically screened, which leaves the possibility that additional regulatory branches may have been overlooked.

5. Conclusions

The present study reveals that *Mir22hg* inhibits Nrf2 signaling pathway activation through competitive binding to *miR-365-2-5p*, thereby exacerbating oxidative stress progression. In contrast, *Mir22hg* knockdown restores *miR-365-2-5p*'s silencing effect on *iNOS*, activates the Nrf2 signaling pathway, and ameliorates oxidative stress. Thus, FNB modulates oxidative stress occurring after PRV infection in RAW 264.7 cells through the *Mir22hg*/*miR-365-2-5p*/*iNOS* ceRNA regulatory axis.

Supplementary Materials: The following supporting information can be downloaded at https://www.mdpi.com/article/10.3390/antiox15111447/s1. Supplementary File S1: Detailed experimental methods of Flavonoid-Targeted Metabolomics and List of primers; Supplementary File S2: Metabolite data.

Author Contributions: Conceptualization, Y.W. and T.H.; data curation, Y.W., W.Z. and H.Y.; formal analysis, W.Z., H.Y. and Q.C.; funding acquisition, T.H.; investigation, Y.W., H.Y., X.Y. and Q.W.; methodology, W.Z. and M.Y.; project administration, Q.C. and T.H.; supervision, T.H.; Visualization, X.Y. and Q.W.; writing—original draft preparation, Y.W.; writing—review and editing, T.H. All authors have read and agreed to the published version of the manuscript.

Funding: This research was funded by the National Natural Science Foundation of China, grant number 32072907, and the Innovation Project of Guangxi Graduate Education, grant number YCBZ2024068.

Institutional Review Board Statement: Approval was obtained from the Ethics Committee of Guangxi University. The institutional animal ethics committee approved the experimental protocol (GXU-2023-0017, approval date: 27 February 2023).

Informed Consent Statement: Not applicable.

Data Availability Statement: The RNA-seq data presented in the study are openly available in the Genome Sequence Archive (GSA), National Genomics Data Center, China National Center for Bioinformation/Beijing Institute of Genomics, Chinese Academy of Sciences (Genomics, Proteomics & Bioinformatics 2025; Nucleic Acids Research 2025). The accession number is CRA044205, and the data are publicly available at https://ngdc.cncb.ac.cn/gsa. Other raw data supporting the conclusions of this article will be made available by the authors upon request.

Conflicts of Interest: The authors declare no conflicts of interest.

References

1. Zheng, H.H.; Fu, P.F.; Chen, H.Y.; Wang, Z.Y. Pseudorabies Virus: From Pathogenesis to Prevention Strategies. *Viruses* **2022**, *14*, 1638. [CrossRef]
2. Chen, Y.; Gao, J.; Hua, R.; Zhang, G. Pseudorabies virus as a zoonosis: Scientific and public health implications. *Virus Genes* **2025**, *61*, 9–25. [CrossRef]
3. Zhao, Y.; Ding, C.; Zhu, Z.; Wang, W.; Wen, W.; Favoreel, H.W.; Li, X. Pseudorabies virus infection triggers mitophagy to dampen the interferon response and promote viral replication. *J. Virol.* **2024**, *98*, e0104824. [CrossRef] [PubMed]
4. Tan, L.; Yao, J.; Yang, Y.; Luo, W.; Yuan, X.; Yang, L.; Wang, A. Current Status and Challenge of Pseudorabies Virus Infection in China. *Virol. Sin.* **2021**, *36*, 588–607. [CrossRef]
5. Bo, Z.; Li, X. A Review of Pseudorabies Virus Variants: Genomics, Vaccination, Transmission, and Zoonotic Potential. *Viruses* **2022**, *14*, 1003. [CrossRef]
6. Hou, Y.; Wang, Y.; Zhang, Y.; Yu, H.; Zhao, Y.; Yi, A. Human Encephalitis Caused by Pseudorabies Virus in China: A Case Report and Systematic Review. *Vector Borne Zoonotic Dis.* **2022**, *22*, 391–396. [CrossRef]
7. Kong, Y.D.; Qi, Y.; Cui, N.; Zhang, Z.H.; Wei, N.; Wang, C.F.; Zeng, Y.N.; Sun, Y.P.; Kuang, H.X.; Wang, Q.H. The traditional herb *Polygonum hydropiper* from China: A comprehensive review on phytochemistry, pharmacological activities and applications. *Pharm. Biol.* **2023**, *61*, 799–814. [CrossRef]
8. Chen, Q.; Wang, Q.; Zhao, Y.; Xie, X.; Feng, H.; Wei, Y.; Yu, M.; Pan, X.; Hu, T. Flavonoids from *Polygonum hydropiper* L. regulate PCV2-induced oxidative stress of RAW264.7 cells via Pi3k/AKT and Nrf2/HO-1 signaling pathways. *Sci. Rep.* **2025**, *15*, 29112. [CrossRef]
9. Tao, J.; Wei, Y.; Hu, T. Flavonoids of *Polygonum hydropiper* L. attenuates lipopolysaccharide-induced inflammatory injury via suppressing phosphorylation in MAPKs pathways. *BMC Complement. Altern. Med.* **2016**, *16*, 25. [CrossRef]
10. Callaway, E.; Sanderson, K. Medicine Nobel awarded for gene-regulating 'microRNAs'. *Nature* **2024**, *634*, 524–525. [CrossRef]
11. Chen, J.; Dai, X.; Xing, C.; Zhang, Y.; Cao, H.; Hu, G.; Guo, X.; Gao, X.; Liu, P.; Yang, F. Cooperative application of transcriptomics and ceRNA hypothesis: lncRNA-00742/miR-116 targets CD74 to mediate vanadium-induced mitochondrial apoptosis in duck liver. *J. Hazard. Mater.* **2024**, *480*, 135904. [CrossRef]
12. Kong, X.; Wang, Q.; Wang, X.; Yang, K.; Nie, S.; Li, Y.; Lao, W.; Yu, X.; Zhang, Y.; Li, Z.; et al. LINC01002 functions as a ceRNA to regulate FRMD8 by sponging miR-4324 for the development of COVID-19. *Virol. J.* **2024**, *21*, 109. [CrossRef]
13. Sheng, B.; Zhao, L.; Zang, X.; Zhen, J.; Liu, Y.; Bian, W.; Chen, W. Quercetin inhibits caerulein-induced acute pancreatitis through regulating miR-216b by targeting MAP2K6 and NEAT1. *Inflammopharmacology* **2021**, *29*, 549–559. [CrossRef]
14. Chen, X.; Zhang, A.; Zhao, K.; Gao, H.; Shi, P.; Chen, Y.; Cheng, Z.; Zhou, W.; Zhang, Y. The role of oxidative stress in intervertebral disc degeneration: Mechanisms and therapeutic implications. *Ageing Res. Rev.* **2024**, *98*, 102323. [CrossRef]
15. Dewan, A.; Jain, C.; Das, M.; Tripathi, A.; Sharma, A.K.; Singh, H.; Malhotra, N.; Seshasayee, A.S.N.; Chakrapani, H.; Singh, A. Intracellular peroxynitrite perturbs redox balance, bioenergetics, and Fe-S cluster homeostasis in *Mycobacterium tuberculosis*. *Redox Biol.* **2024**, *75*, 103285. [CrossRef]
16. Wei, Y.H.; Zhou, S.M.; Zhao, W.; Chen, Q.; Wang, Q.H.; Yu, M.L.; Wei, Y.Y.; Hu, T.J. Normal butanol fraction of *Polygonum hydropiper* L. flavonoids reduces inflammation caused by PCV2 infections in cell and mouse models. *Front. Vet. Sci.* **2025**, *12*, 1539448. [CrossRef]
17. Zhao, Y.; Qi, X.; Zhu, Z.; Wang, W.; Wen, W.; Li, X. Increased ROS levels activate AMPK-ULK1-mediated mitophagy to promote pseudorabies virus replication. *Vet. Res.* **2025**, *56*, 156. [CrossRef]
18. Marcaccini, A.; López-Peña, M.; Bermúdez, R.; Quiroga, M.I.; Guerrero, F.H.; Nieto, J.M.; Alemañ, N. Pseudorabies virus induces a rapid up-regulation of nitric oxide synthases in the nervous system of swine. *Vet. Microbiol.* **2007**, *125*, 232–243. [CrossRef]
19. Lin, H.W.; Lee, Y.J.; Yang, D.J.; Hsieh, M.C.; Chen, C.C.; Hsu, W.L.; Chang, Y.Y.; Liu, C.W. Anti-inflammatory effects of Flos Lonicerae Japonicae Water Extract are regulated by the STAT/NF-κB pathway and HO-1 expression in Virus-infected RAW264.7 cells. *Int. J. Med. Sci.* **2021**, *18*, 2285–2293. [CrossRef]

20. Huan, C.; Yang, F.; Zhang, W.; Yan, P.; Yao, J.; Jiang, L.; Gao, S. Antiviral activity and antioxidant activity of *Cistanche deserticola* polysaccharides against pseudorabies viruses. *Int. J. Biol. Macromol.* **2025**, *321*, 146326. [CrossRef]
21. Nasir, A.; Khan, M.; Rehman, Z.; Khalil, A.A.K.; Farman, S.; Begum, N.; Irfan, M.; Sajjad, W.; Parveen, Z. Evaluation of Alpha-Amylase Inhibitory, Antioxidant, and Antimicrobial Potential and Phytochemical Contents of *Polygonum hydropiper* L. *Plants* **2020**, *9*, 852. [CrossRef]
22. Bairagi, J.; Saikia, P.J.; Boro, F.; Hazarika, A. A review on the ethnopharmacology, phytochemistry and pharmacology of *Polygonum hydropiper* Linn. *J. Pharm. Pharmacol.* **2022**, *74*, 619–645. [CrossRef]
23. Ren, C.Z.; Hu, W.Y.; Li, J.C.; Xie, Y.H.; Jia, N.N.; Shi, J.; Wei, Y.Y.; Hu, T.J. Ethyl acetate fraction of flavonoids from *Polygonum hydropiper* L. modulates pseudorabies virus-induced inflammation in RAW264.7 cells via the nuclear factor-kappa B and mitogen-activated protein kinase pathways. *J. Vet. Med. Sci.* **2020**, *82*, 1781–1792. [CrossRef]
24. Chen, D.; Liu, J.; Yan, H.; Yuan, Q.; Zhan, H.; Ai, Y.; Wang, X.; Chen, Y.; Shi, L.; Zhang, Y. *Polygonum hydropiper* L. ethanol extract attenuates ferroptosis and ulcerative colitis by modulating glutathione metabolism through inhibition of KEAP1-Nrf2 interaction. *Phytomedicine* **2025**, *146*, 157096. [CrossRef]
25. Liu, C.W.; Lin, H.W.; Yang, D.J.; Chen, S.Y.; Tseng, J.K.; Chang, T.J.; Chang, Y.Y. Luteolin inhibits viral-induced inflammatory response in RAW264.7 cells via suppression of STAT1/3 dependent NF-κB and activation of HO-1. *Free Radic. Biol. Med.* **2016**, *95*, 180–189. [CrossRef]
26. Jiang, J.; Wei, Y.; Zhao, W.; Yuan, H.; Huang, C.; Yu, X.; Li, Y.; Jiang, L.; Yu, M.; Hu, T.; et al. Regulatory mechanism of quercitrin on oxidative stress and histone acetylation changes in PRV infected 3D4/2 cells. *Microb. Pathog.* **2025**, *208*, 107958. [CrossRef]
27. Cao, M.X.; Xie, X.D.; Wang, X.R.; Hu, W.Y.; Zhao, Y.; Chen, Q.; Ji, L.; Wei, Y.Y.; Yu, M.L.; Hu, T.J. Separation, Purification, Structure Analysis, In Vitro Antioxidant Activity and circRNA-miRNA-mRNA Regulatory Network on PRV-Infected RAW264.7 Cells of a Polysaccharide Derived from *Arthrospira platensis*. *Antioxidants* **2021**, *10*, 1689. [CrossRef]
28. Zhen, J.; Chen, W.; Liu, Y.; Zang, X. Baicalin Protects Against Acute Pancreatitis Involving JNK Signaling Pathway via Regulating miR-15a. *Am. J. Chin. Med.* **2021**, *49*, 147–161. [CrossRef]
29. Salman, R.M.; Radwan, A.F.; Shaker, O.G.; El-Husseiny, A.A. LncRNA MIR22HG and miR-10a-5p: Pioneering serum biomarkers for pancreatic cancer diagnosis and progression assessment. *Noncoding RNA Res.* **2026**, *20*, 16–28. [CrossRef]
30. Wei, Z.; Li, X.; Zhou, J.; Zhou, Y.; Xiao, Z.; Yang, Q.; Liu, X.; Peng, Y.; Yang, Y.; Ding, Y.; et al. Inhibition of miRNA-365-2-5p Targeting SIRT1 Regulates Functions of Keratinocytes to Enhance Wound Healing. *FASEB J.* **2025**, *39*, e70560. [CrossRef]
31. Michalak, K.P.; Michalak, A.Z. Understanding chronic inflammation: Couplings between cytokines, ROS, NO, Ca_i^{2+}, HIF-1α, Nrf2 and autophagy. *Front. Immunol.* **2025**, *16*, 1558263. [CrossRef]
32. Kang, C.H.; Choi, Y.H.; Moon, S.K.; Kim, W.J.; Kim, G.Y. Quercetin inhibits lipopolysaccharide-induced nitric oxide production in BV2 microglial cells by suppressing the NF-κB pathway and activating the Nrf2-dependent HO-1 pathway. *Int. Immunopharmacol.* **2013**, *17*, 808–813. [CrossRef]

Disclaimer/Publisher's Note: The statements, opinions and data contained in all publications are solely those of the individual author(s) and contributor(s) and not of MDPI and/or the editor(s). MDPI and/or the editor(s) disclaim responsibility for any injury to people or property resulting from any ideas, methods, instructions or products referred to in the content.